GLIA

WILEY

RESEARCH ARTICLE

Retinal regions shape human and murine Müller cell proteome profile and functionality

Lew Kaplan[1] | Corinne Drexler[2,3] | Anna M. Pfaller[1] | Santra Brenna[4] |
Kirsten A. Wunderlich[1] | Andrea Dimitracopoulos[5] | Juliane Merl-Pham[6] |
Maria-Theresa Perez[7,8] | Ursula Schlötzer-Schrehardt[9] | Volker Enzmann[10,11] |
Marijana Samardzija[12] | Berta Puig[4] | Peter Fuchs[2] | Kristian Franze[5,13,14] |
Stefanie M. Hauck[6] | Antje Grosche[1]

[1]Department of Physiological Genomics, Ludwig-Maximilians-Universität München, Munich, Germany

[2]Max Perutz Labs, Department of Biochemistry and Cell Biology, University of Vienna, Vienna Biocenter Campus (VBC), Vienna, Austria

[3]Vienna Biocenter PhD Program, Doctoral School of the University of Vienna and Medical University of Vienna, Vienna, Austria

[4]Neurology Department, Experimental Research in Stroke and Inflammation (ERSI), University Medical Center Hamburg-Eppendorf, Hamburg, Germany

[5]Department of Physiology, Development and Neuroscience, University of Cambridge, Cambridge, UK

[6]Research Unit Protein Science and Metabolomics and Proteomics Core, Helmholtz Zentrum München, German Research Center for Environmental Health, Neuherberg, Germany

[7]Department of Clinical Sciences, Division of Ophthalmology, Lund University, Lund, Sweden

[8]NanoLund, Nanometer Structure Consortium, Lund University, Lund, Sweden

[9]Department of Ophthalmology, Friedrich-Alexander-Universität Erlangen-Nürnberg, Erlangen, Germany

[10]Department of Ophthalmology, Bern University Hospital, Inselspital, University of Bern, Bern, Switzerland

[11]Department of BioMedical Research, University of Bern, Bern, Switzerland

[12]Department of Ophthalmology, University Hospital Zurich, University of Zurich, Zurich, Switzerland

[13]Institute of Medical Physics, Friedrich-Alexander-Universität Erlangen-Nürnberg, Erlangen, Germany

[14]Max-Planck-Zentrum für Physik und Medizin, Erlangen, Germany

Correspondence

Antje Grosche, Department of Physiological Genomics, Ludwig-Maximilians-Universität München, Munich, Germany.
Email: antje.grosche@med.uni-muenchen.de

Abstract

The human macula is a highly specialized retinal region with pit-like morphology and rich in cones. How Müller cells, the principal glial cell type in the retina, are adapted to this environment is still poorly understood. We compared proteomic data from cone- and rod-rich retinae from human and mice and identified different expression profiles of cone- and rod-associated Müller cells that converged on pathways representing extracellular matrix and cell adhesion. In particular, epiplakin (EPPK1), which is thought to play a role in intermediate filament organization, was highly expressed in macular Müller cells. Furthermore, *EPPK1* knockout in a human Müller cell-derived cell line led to a decrease in traction forces as well as to changes in cell size, shape, and filopodia characteristics. We here identified EPPK1 as a central molecular player in the region-specific architecture of the human retina, which likely enables specific functions under the immense mechanical loads in vivo.

1 | INTRODUCTION

A healthy retina is our most important gateway to the outside world, providing us with a major part of our sensory input to orient and interact with our environment quickly and efficiently (Hutmacher, 2019). For sharp vision in humans, most of the image information is focused on a tiny spot of the retina, the macula. Therefore, any damage in this area has catastrophic effects. The macula with its central fovea is characterized by a pit-like depression in which the somata of the inner retinal cells are displaced laterally so that light can strike the photoreceptors unimpeded. The outer nuclear layer in this region is increasingly dominated by cones. This culminates in the foveola, which contains almost exclusively cones, surrounded and supplied only by processes of a z-shaped subpopulation of Müller cells, the major macroglia of the retina. Finally, the retinal vasculature is completely absent from the fovea (Bringmann et al., 2018) and increased light exposure leads to a higher turn-over in metabolites and the production of reactive oxygen species (Handa, 2012).

Many known pathologies leading to visual impairment are caused by defects in photoreceptor, vasculature, or the retinal pigment epithelium (RPE) functions, which have been intensively studied in recent decades (Bhutto & Lutty, 2012; Lenis et al., 2018; Verbakel et al., 2018). In contrast, despite their numerous important functions, Müller cells are still poorly understood. Originally thought to provide mainly structural support for retinal neurons, it has later been proposed that Müller cells shuttle not only metabolites like pyruvate and lactate, but are, to name just a few examples, also involved in glutamate recycling—similar to brain astrocytes (Hurley et al., 2015; Lu et al., 2006; Reichenbach & Bringmann, 2020; Toft-Kehler et al., 2018)—or even glutamate release to feedback on neurons (Slezak et al., 2012). Such functions are mediated by a myriad of Müller cell processes contacting all other retinal cell types. In addition, Müller glia, which extend across the entire thickness of the retina, are thought to conduct light through all cell layers to the photoreceptors on the light-averted side of the retina (Franze et al., 2007) and to be responsible not only for the biomechanical stability of the tissue, but also for the formation of the foveal pit (Bringmann et al., 2018; Bringmann et al., 2020; MacDonald et al., 2015). In zebrafish, it has been shown that Müller cells can acquire stem cell properties after injury, leading to complete tissue regeneration (Goldman, 2014; Wan & Goldman, 2016). Finally, while the canonical visual cycle involves the multistep enzymatic conversion of all-trans-retinol to 11-cis-retinal in the RPE, an alternative, cone-specific and Müller cell-dependent pathway has been described recently (Wang & Kefalov, 2011).

Although it is conceivable that the unique conditions of the human macula pose challenges for both photoreceptors and Müller cells, many of these aspects have been studied in model systems that do not have the specifics of this region. This raises the question of how glial metabolism and metabolite exchange adapt to increased energy consumption, increased cone density, and lack of vascularization in the macula. Alternatively, what factors are necessary to provide the extremely long, Z-shaped Müller cells of the macula with the biomechanical properties needed to withstand the high mechanical stresses and tensile forces imposed by the vitreous to preserve the fragile tissue structure of this retinal region (Bringmann et al., 2021). To approach these questions at a broad molecular level, transcriptomic and especially proteomic profiling of human Müller cells are required. There have been efforts to use bulk RNA sequencing (RNAseq) (Whitmore et al., 2014), which provides excellent depth but is unable to distinguish between cell types, so that only general interregional differences are represented, an obstacle that has been solved by the advent of single-cell (sc)RNAseq (Chambers et al., 2019; Voigt et al., 2021). However, it is important to bear in mind that the final products in the cell are, in most cases, proteins that coordinate cellular metabolism, structural integrity, and intercellular communication. Many steps influence how much of the final functional protein results from a specific mRNA. These include regulation of mRNA translation, post-translational modifications, oligomerization, and stability issues of both the mRNA and the protein. However, whole retina mass proteomic analysis suffers from similar limitations as bulk RNAseq and single-cell proteomics is still under development (Brunner et al., 2022; Kelly, 2020). To tackle these challenges, we previously established a method to isolate pure, morphologically intact Müller cells from murine (Grosche et al., 2016) or human retina. We compared the proteomes of Müller cells isolated from the R91W/Nrl$^{-/-}$ mice, representing Müller cells in a cone-rich environment similar to the macula, with the proteomes of control mice, representing Müller cells in the peripheral human retina, and of human Müller cells isolated from the macula and periphery. We found differentially expressed proteins converging on specific molecular pathways—a number of which were the same in both species. EPPK1, a selected novel protein candidate, was functionally characterized by studying a respective knockout in the human Müller cell-derived cell line MIO-M1. Our results indicate that EPPK1 participates in the constitution of macular Müller cell's tensile strength as well as morphology and has an influence on the secretion of extracellular vesicles.

The identification of the molecular and functional properties of retinal Müller cells of the macula is urgently needed to better understand and efficiently fight debilitating sight-threatening diseases in humans such as age-related macular degeneration. With this study, we provide the first insights into the heterogeneity of human retinal Müller cells at a protein level and point to potential directions for future research.

2 | MATERIALS AND METHODS

2.1 | Mouse lines and donor tissue

The all-cone Rpe65R91W;Nrl$^{-/-}$ (R91W;Nrl) mouse model (Samardzija et al., 2014) and the Rpe65R91W single mutant mice (Samardzija et al., 2008) were bred at a specific pathogen-free barrier animal facility of the Helmholtz Center Munich in accordance with and with allowance by institutional as well as state and federal guidelines (5.1–568-Gas: Allowance to breed and kill animals for scientific purposes).

Eppk1 knockout mice of the C57BL/6 background (Spazierer et al., 2006; Szabo et al., 2015) and C57BL/6 wild-type mice were kept at the pathogen-free mouse facility of the Max Perutz Labs animal facility, Vienna, Austria, in accordance with Austrian Federal Government laws.

Eyes from adult male and female mice (3 to 6 months of age) were collected after animals were sacrificed via cervical dislocation. Eyes fixed in 4% PFA from *Gfap/Vim* double knockout mice (3 months of age) were kindly provided by Maria-Theresa Perez (Lund University, Lund, Sweden).

Samples for proteome profiling of human Müller cells were isolated from a set of five donor eyes. The Institutional Review Board at University of Regensburg approved the use of human tissues for this purpose. Five eyes from four non-diabetic Caucasian donors 58–89 years of age (2 males, 1 female, 1 of unknown gender) at a death-to-experimentation interval of <30 h were included in this analysis (Figure S1, Table S1). Ocular health histories were not available. Eyes were opened by eye bank recovery personnel using an 18 mm diameter corneal trephine and stored on ice for transfer to the laboratory for further processing.

To stain for EPPK1 in the macular and peripheral retina, human eyes (postmortem time <8–24 h, two eyes from two donors, Table S1) were cryosectioned. The research complies with the human research act (HRA) stating that small quantities of bodily substances removed in the course of transplantation may be anonymized for research purposes without consent (HRA chapter 5, paragraph 38, Switzerland).

2.2 | Proteomic profiling of MACS enriched retinal cell types

2.2.1 | Cell purification from human donor or murine retina

As described previously (Grosche et al., 2016), different retinal cell types were isolated either from whole murine retina or from 6 mm punches (from macula and from periphery) of human retina using magnetic activated cell sorting. First, the tissue was treated with papain (0.2 mg/ml; Roche) for 30 min at 37°C in PBS/Glucose (12 mM), washed and incubated in DNase I (200 U/ml in PBS/Glucose) for 4 min at RT. PBS/Glucose was removed and substituted with

extracellular solution (ECS, 136 mM NaCl, 3 mM KCl, 10 mM HEPES, 11 mM glucose, 1 mM MgCl$_2$ and 2 mM CaCl$_2$, pH 7.4) before dissociating the tissue using a firepolished glass Pasteur pipette. The cell suspension was sequentially depleted of microglia and vascular cells by incubating (15 min, 4°C) with anti-mouse/human CD11b and CD31 microbeads (Miltenyi Biotec), respectively, and passing through LS-columns according to manufacturer's protocol (Miltenyi Biotec). The resulting suspension was incubated (15 min, 4°C) with anti-CD29 biotinylated antibodies (0.1 mg/ml, Miltenyi Biotec), spun down, washed and the pellet resuspended in ECS containing anti-biotin ultra-pure MicroBeads (1:5; Miltenyi Biotec). The suspension was passed through a LS-column resulting in a neuron-rich flowthrough (CD29$^-$), before the bound CD29$^+$ Müller cells were finally eluted from the column. To prepare samples for immunostaining, 100 μl of each of the CD29$^+$ and CD29$^-$ fractions were fixed for 15 min in 4% paraformaldehyde (PFA) at RT, spun down, resuspended in 50 μl PBS and dropped onto a microscope slide.

2.2.2 | LC–MS/MS mass spectrometry analysis

Proteins were proteolysed with LysC and trypsin with filter-aided sample preparation procedure (FASP) as described (Grosche et al., 2016; Wiśniewski et al., 2009). Acidified eluted peptides were analyzed on a QExactive HF or HF-X mass spectrometer (Thermo Fisher Scientific) online coupled to a Ultimate 3000 RSLC nano-HPLC (Dionex) as described (Grosche et al., 2016). Briefly, samples were automatically injected and loaded onto the C18 trap cartridge and after 5 min eluted and separated on the C18 analytical column (nanoEase MZ HSS T3, 100 Å, 1.8 μm, 75 μm × 250 mm; Waters) by a 95 min nonlinear acetonitrile gradient at a flow rate of 250 nl/min. MS spectra were recorded at a resolution of 60,000 with an automatic gain control (AGC) target of 3e6 and a maximum injection time of 30 or 50 ms from 300 to 1500 m/z. From the MS scan, the 10 or 15 most abundant peptide ions were selected for fragmentation via HCD with a normalized collision energy of 27 or 28, an isolation window of 1.6 m/z, and a dynamic exclusion of 30 s. MS/MS spectra were recorded at a resolution of 15,000 with a AGC target of 1e5 and a maximum injection time of 50 ms. Unassigned charges, and charges of +1 and > +8 were excluded from precursor selection.

Acquired raw data were analyzed in the Proteome Discoverer software (versions 2.2 or 2.4, Thermo Fisher Scientific) for peptide and protein identification via a database search (Sequest HT search engine) against the SwissProt Mouse database (Release 2020_02, 17,061 sequences) or the SwissProt Human database (Release 2020_02, 20,435 sequences), considering full tryptic specificity, allowing for up to one missed tryptic cleavage site, precursor mass tolerance 10 ppm, fragment mass tolerance 0.02 Da. Carbamidomethylation of cysteine was set as a static modification. Dynamic modifications included deamidation of asparagine and glutamine, oxidation of methionine, and a combination of methionine loss with acetylation on protein N-terminus. The Percolator algorithm (Käll et al., 2007) was used for validating peptide spectrum matches and peptides. Only top-scoring identifications

for each spectrum were accepted, additionally satisfying a false discovery rate < 1% (high confidence). The final list of proteins satisfying the strict parsimony principle included only protein groups passing an additional protein confidence false discovery rate < 5% (target/decoy concatenated search validation).

Quantification of proteins, after precursor recalibration, was based on intensity values (at RT apex) for all unique peptides per protein. Peptide abundance values were normalized on total peptide amount. The protein abundances were calculated summing the abundance values for admissible peptides. The final protein ratio was calculated using median abundance values of five biological replicates each. The statistical significance of the ratio change was ascertained with ANOVA. For the MIO-M1 data sets, the statistical significance of the ratio change was ascertained employing the *t* test approach described in (Navarro et al., 2014) which is based on the presumption that we look for expression changes for proteins that are just a few in comparison to the number of total proteins being quantified. The quantification variability of the non-changing "background" proteins can be used to infer which proteins change their expression in a statistically significant manner.

2.3 | EV isolation from cell culture media and NTA analysis

After 72 h incubation, serum-free media was collected from both WT and *EPPK1* knockout MIO-M1 cells and immediately centrifuged at $300 \times g$, for 10 min at 4°C. The resulting supernatant was then centrifuged at $2000 \times g$, for 10 min at 4°C. The resulting supernatant was further centrifuged at $10.000 \times g$, for 30 min at 4°C. Lastly, the $10.000 \times g$ supernatant was spun at $100.000 \times g$ (24.000 rpm, sw40ti rotor) for 70 min at 4°C. The final pellet was resuspended in 30 μl PBS with protease inhibitors (Roche). The cell numbers were assessed for each replicate well.

The final EVs suspension was diluted either 1:300 (WT) or 1:100 (KO cell lines). The measurement was done with the LM10 unit (Nanosight). The diluted samples were recorded with 10 videos, each 10 s long. Data analysis with NTA 3.0 software (Nanosight) was performed with the following settings: detection threshold = 6, screen gain = 2. Particle numbers were adjusted for dilution as well as cell number.

2.4 | Immunofluorescence staining and microscopy

Mouse eyes were fixed in 4% PFA for 1 h, cryoprotected, embedded in OCT compound and cut into sections of 20 μm thickness using a cryostat. Human donor eyes were immersion-fixated with 4% paraformaldehyde (PFA) for 48 h. Thereafter, the central part of the eye cup containing the optic nerve head and the macula including the underlying RPE, choroid, and sclera was dissected. The tissue was submitted to cryoprotection, embedded in OCT and cut into 20 μm thick sections. Retinal detachment from the RPE is an artifact commonly observed in cryosections.

Retinal sections were permeabilized (0.3% Triton X-100 plus 1.0% DMSO in PBS) and blocked (5% normal donkey serum with 0.3% Triton X-100 and 1.0% DMSO in PBS) for 2 h at room temperature. Primary antibodies (Table 1) were incubated overnight at 4°C. Sections were washed (1% bovine serum albumin [BSA] in PBS) and incubated with secondary antibodies (2 h at room temperature; Table 2). Cell nuclei were labeled with DAPI (1:1000; Life Technologies). Control experiments without primary antibodies showed no nonspecific labeling.

MIO-M1 cells were grown on sterile coverslips until desired confluency, washed with PBS and fixed for 15 min in 4% PFA. Cells were then permeabilized with 0.1% Triton X-100 in PBS for 10 min, washed with 1% BSA/PBS and incubated with primary antibodies for 2 h at RT. Coverslips were subsequently washed with PBS and incubated with secondary antibodies and DAPI for 1.5 h at RT and lastly mounted onto a microscope slide.

Confocal images were taken with a custom-made VisiScope CSU-X1 confocal system (Visitron Systems) equipped with high-resolution sCMOS camera (PCO AG).

Stimulated emission depletion (STED) microscopy was performed at the Core Facility Bioimaging of the Biomedical Center with an inverted Leica SP8X STED 3D microscope, equipped with a 405 nm Laser and a pulsed white light laser (470–670 nm). Gated-STED images were acquired with a 93x/1.30 glycerol objective, pixel size was around 30–32 nm. The following spectral settings were used: Abberior Star 580 (ex: 580 nm; em: 590–620 nm) and Abberior STAR 635P (ex: 635 nm; em: 645–702 nm). Signals were recorded with hybrid photo detectors (HyDs) in counting mode. Depletion laser wavelength was 775 nm.

2.5 | qPCR

Total RNA was isolated from peripheral retinal samples of three donors and from wild type MIO-M1 cells using PureLink™ RNA Mini Kit (ThermoFisher, 12183018A) following manufacturer's instructions; 50 ng of total RNA per sample were reverse transcribed with RevertAid Reverse Transcriptase (ThermoFisher, EP0441) with the help of random hexamer primers. Primers for qPCR were designed using the Universal ProbeLibrary Assay Design Center (Roche) to be used with the corresponding probes (Table 2). Since *EPPK1* mRNA consists of only one translated exon, an exon spanning assay was not possible. Final expression values were calculated via the ΔCt method by taking the difference between *EPPK1* and a house keeper's (*PDHB*) Ct values and using the result as the power of two.

2.6 | Western blot analysis

A 100% confluent 10 cm cell culture dish was used for isolating protein lysates. The cells were washed two times with PBS and subsequently overlaid with 500 μl of ice-cold protein lysis buffer (50 mM HEPES pH 7, 100 mM NaCl, 5 mM $MgCl_2$, 1 mM EGTA or EDTA,

TABLE 1 Antibodies used for immunofluorescence stainings

Primary antibody	Species	Company	Catalogue number/reference	Dilution/concentration
GLUL	Mouse	Merck	MAB302	1:500
CD9	Rat	BD Biosciences	553758	1:200
GFAP	Mouse	Sigma-Aldrich	G3893	1:500
EPPK1	Rabbit	gift from G. Wiche (Spazierer et al., 2003)	-	1:2000
VIM	Mouse	Santa Cruz	sc-373717	1:500
Secondary antibody				
Anti-rabbit-Cy3	Goat	Dianova	111-165-144	1:500
Anti-mouse-AF488	Goat	LifeTech	A-1109	1:500
Anti-rat-Cy3	Goat	Dianova	112-165-167	1:500
Anti-mouse-Abberior STAR 580	Goat	Abberior	2-0002-005-1	1:200
Anti-rabbit-Abberior STAR 635P	Goat	Abberior	2–0012–007-2	1:200

TABLE 2 qPCR primers

Primer	UPL probe #	Sequence (5′–3′)
h_EPPK1_qpcr_for	32	CCACAAGAAGAGCTTTTTCCAG
h_EPPK1_qpcr_rev	32	AGCCTGGGCCTCTAGGAGT
h_PDHB_qpcr_for	17	AGAGGCGCTTTCACTGGAC
h_PDHB_qpcr_rev	17	CCAAGCAGAAATACCTTCTCATC

2.5% Triton X-100, 100 nM DTT, 0.5 mg/ml DNaseI, 0.2 mg/ml RNase A, 1 mM PMSF, protease inhibitors [cOmplete ULTRA tablets, Roche]) before scraping them off. The solution was homogenized, transferred into an Eppendorf tube, and incubated for 5 min at room temperature and lastly sheared via a 27-gauge needle. For retinal samples, the tissue was snap frozen in liquid nitrogen and per 10 mg of tissue 200 μl of tissue protein lysate buffer (Tris pH 7.5; 10 mM NaCl; 150 mM EDTA; 5 mM Triton X-100; 1% SDS; 0.1% NP-40; 1% 1% phosphatase inhibitor cocktails 2 and 3 [Sigma–Aldrich, cat no. P5726 and P0044]; 100 μg/ml DNAse I; 100 μg/ml RNAse; 1 mM PMSF) was added. The tissue was homogenized using an IKA® ULTRA-TUR-RAX® disperser tool (IKA T10 basic), until a homogenized solution was observed. The suspension was incubated for 10 min at RT with periodic mixing to guarantee efficient cell lysis and ribonuclease digestion.

Samples were combined with SDS loading dye (390 mM Tris–HCl pH 6.8, 485 mM DTT, 10% SDS, 0.1% Bromophenol-Blue, 50% glycerol) and incubated at 95°C for 5 min before clearing the samples by centrifugation at 13800 g. Equal sample volumes were run on a 12% gel and stained with Coomassie dye to account for loading differences (Figure S2). Next, samples were loaded onto a combination of a stacking (4%) and resolving (6%) SDS polyacrylamide gel. The electrophoresis was run at 20 mA per gel until 1 h after the dye front ran out and the 250 kDa band of the protein ladder reached the bottom of the gel. Protein was transferred to a nitrocellulose membrane using a Mini

Trans-Blot machine (Biorad) at 4°C, 25 V overnight. Membranes were blocked in 5% BSA/PBS for 1 h, washed with PBS/0.05% Tween20 (PBS-T), and incubated with primary antibody diluted in 5% BSA/PBS-T for 3 hours at RT. After washing the membrane again and incubating it with HRP-conjugated secondary antibody (goat anti-rabbit, 1:20000, Vector Laboratories), protein bands were visualized using Clarity Max Western ECL Substrate (Biorad, 1705060 S). For human cell lines, we used a rabbit anti-EPPK1 primary antibody acquired from Thermo Fisher (PA5-66869) in a dilution of 1:2000, while samples stemming from mouse tissue were incubated with a rabbit anti-EPPK1 antibody (dilution 1:10000) generated in an earlier study (Spazierer et al., 2003).

2.7 | Cell culture and CRISPR approach to generate a *EPPK1* knockout

MIO-M1 cells (Limb et al., 2002) were cultured in FBS containing medium (DMEM, high glucose, GlutaMAX™ Supplement, HEPES, 10% FBS, 1:100 Penicillin/Streptomycin; Gibco) at 37°C, 5% CO₂ unless stated otherwise.

We generated an *EPPK1* knockout in MIO-M1 cells using pSpCas9(BB)-2A-Puro (PX459) V2.0 plasmid supplied by Addgene (plasmid # 6298) as suggested by the authors that deposited the plasmid (Ran et al., 2013). We first designed gRNAs using various tools (Benchling, (2021), CRISPRdirect (Naito et al., 2015)) targeted at a 1000 bp long region in the beginning of the translated exon and chose two guides each with minimal off-site reactivity (Table 3). Restriction digest of the plasmid with BbsI-HF (NEB) and subsequent ligation (T4 DNA Ligase, NEB) with the annealed, double stranded oligonucleotides yielded the final expression vectors, the correctness of which was confirmed by sequencing.

For the transfection, ~300,000 cells were seeded per well of a 6-well plate to receive a subconfluent culture on the next day. Cells were transfected with an equimolar mix of all four vectors using

TABLE 3 Guide RNAs designed for EPPK1 knockout in human MIO-M1 cells

	Designed gRNA sequence (5′–3′)	Strand	Tool	Oligonucleotides ready for cloning (5′–3′)
gRNA_1_top	GGCTATCCTGACCCCTACGG	+	Benchling	caccGGCTATCCTGACCCCTACGG
gRNA_1_bottom				aaacCCGTAGGGGTCAGGATAGCC
gRNA_2_top	ACGTGCACTCACGTCCACTG	−	Benchling	caccGACGTGCACTCACGTCCACTG
gRNA_2_bottom				aaacCAGTGGACGTGAGTGCACGTC
gRNA_3_top	CCAGAGTGTCTACGCCGCCA	+	CRISPRdirect	caccGCCAGAGTGTCTACGCCGCCA
gRNA_3_bottom				aaacTGGCGGCGTAGACACTCTGGC
gRNA_4_top	CCTGGAGGGTACCGGCAGCG	+	CRISPRdirect	caccGCCTGGAGGGTACCGGCAGCG
gRNA_4_bottom				aaacCGCTGCCGGTACCCTCCAGGC

Note: Lowercase letters indicate overhangs necessary for correct insertion into the digested vector backbone and are not part of the target sequence. A 5′ G (underlined) was added to guides if not already present to increase transcription efficiency by the U6 promoter (Ran et al., 2013).

TABLE 4 Primers used to verify construct and knockout sequence

Primer	Usage	Sequence (5′–3′)
hU6-F	Vector sequencing	GAGGGCCTATTTCCCATGATT
hEPPK1_PCRSeq_for	Target region amplification and sequencing	TAACCAGCCGTGTGTGATGAGT
hEPPK1_PCRSeq_rev	Target region amplification and sequencing	CCTGTCCACTAGCCCCTTCTTC

jetOPTIMUS transfection reagent (Polyplus) according to manufacturer's protocol. Briefly, a total of 2.5 μg of plasmid mix was added to 200 μl of jetOPTIMUS buffer, which then was supplemented with 2.5 μl jetOPTIMUS reagent and incubated for 10 min. This transfection mix was added to the cells and incubated for 4 hours before exchanging the medium. Cells were allowed to recover for 48 h before moving to puromycin (3 μg/ml) containing selection medium. After 4 days the remaining transfected cells were harvested and seeded in a 96-well plate at a density of 5 cells/ml (100 μl containing 0.5 cells per well) ensuring that most wells would contain either zero or one cell. Thus, colonies grown in such wells would be originating from a single cell and yield monoclonal cell lines. After ∼3 weeks, we saw colonies big enough to be harvested and further expanded two of them in bigger scale thereby generating the final monoclonal cell lines F7 and C9. Genomic DNA was isolated from these lines and used as input for a PCR with primers amplifying the 1000 bp target region in order to confirm the knockout on genomic level via sequencing (Table 4).

2.8 | Traction force microscopy

To perform traction force microscopy, we first produced acrylamide-based gels with a defined shear modulus of 1000 Pa as previously published by Bollmann et al. (2015) and applied them to culture dishes. Briefly, glass bottom dishes (μ-Dish 35 mm, high, Ibidi) were first treated with (3-Aminopropyl) trimethoxysilane (APTMS) for 2–3 min and washed with distilled water. The glass surface was then covered with 2.5% glutaraldehyde for 30 min, washed and air-dried. Coverslips were prepared by cleaning in 80% ethanol and water and made hydrophobic by submerging them in RainX (Kraco Car Care International Ltd.) for 10 min. For the gels, we first made a master mix by combining 500 μl 40% acrylamide (Sigma-Aldrich) with 65 μl hydroxy-acrylamide (Sigma-Aldrich); 500 μl of this solution was added to 250 μl 2% bis-acrylamide (Fisher Scientific) to obtain the final master mix. In order to produce gels of 1000 Pa stiffness we mixed 75 μl master mix with 415 μl sterile PBS and 10 μl fluorescent beads (FluoSpheres carboxylate, 0.2 μm, crimson, Life Technologies). To ensure even dispersion of the beads, the gel solution was placed in an ultrasonic bath for 5 min and subsequently degassed in a desiccator for 10 min. Polymerization was initiated by the addition of 5 μl 10% APS and 1.5 μl of TEMED before adding 10 μl of the solution onto the treated glass bottom. By placing the prepared coverslip on top of the drop and immediately inverting the dish, we ensured an even distribution of the gel and the placement of the beads close to the imaging surface. After polymerization, PBS was added to the dish and the coverslip removed.

Two milliliter of a cell suspension containing 20,000 cells were seeded onto the gels and cultured over night before imaging. The dishes were imaged at the Core Facility Bioimaging of the Biomedical Center using an inverted Leica DMi8 Widefield microscope equipped with a Hamamatsu-Flash4 camera and a Lumencor SpectraX light engine using a 40x/0.60 objective. A motorized stage enabled the precise marking and revisiting of specific spots on the dish while an incubator enclosure and heated dish holder ensured cell culture conditions (37°C, 5% CO_2); 10 to 20 cells exhibiting a clear non-round morphology were selected per dish: Each cell position was scanned with phase contrast additionally to the fluorescence imaging (ex.: 625–655 nm, em.: 670–770 nm) to detect the location of the cell and the beads in the associated state. Gels were rinsed with PBS, incubated with trypsin, and rigorously rinsed again to ensure complete cell detachment but taking care not to move the dish. All positions were revisited to document the embedded beads in their relaxed state as well as the absence of the cell.

To calculate the traction stress and generate traction force maps we used several plugins for the ImageJ (Schindelin et al., 2012) software as well as custom written macros. Images of the beads were first enhanced in contrast, and then combined into a stack of which the background was subtracted using the rolling ball algorithm. The *Linear Stack Alignment with SIFT* (Lowe, 2004) plugin was then used to align both images of the stack to account for the x,y-drift when revisiting the cell positions. Next, each stack was processed with a plugin for particle image velocimetry (PIV) (Tseng, 2011; Tseng et al., 2012) using the template matching method with advanced settings. Traction forces and corresponding heat maps were calculated from the PIV vector matrices using a plugin for Fourier-transform traction cytometry (FTTC) (Tseng, 2011; Tseng et al., 2012). In some cases, the x,y-drift caused excessively high forces to be detected at the edges of a traction map, which is why we excluded all values in a 335-pixel wide frame. From the remaining values we calculated the average traction stress as the mean of all forces above a threshold set at 30% of the maximum value (peak traction stress) for each image analogous to the protocol developed by Bollmann et al. (2015). The custom ImageJ macros including the specific settings for the SIFT, PIV, and FTTC plugins are available upon request.

2.9 | Bioinformatic and statistical analyses

All statistical analyses were performed using the R programming language unless stated otherwise.

For differential protein expression analysis, we first excluded proteins that had missing values in more than two out of five Müller cell samples per group. Then, we chose only proteins that were significantly enriched in Müller cells in at least one group (RMG/neuron ratio >1, adjusted p-value <.05) yielding the Müller cell-specific proteins. The normalized abundance values were log transformed and used as an input to calculate differential protein expression with the limma package (Ritchie et al., 2015). PCA coordinates were calculated on log transformed normalized abundance values as input of the *prcomp* function and subsequently visualized via the factoextra (Kassambara & Mundt, 2020) package. Heat maps were produced on the basis of median centered, log transformed normalized abundances using the pheatmap (Kolde, 2019) package. Other plots were created with ggplot2 (Data S1).

Single-cell RNA sequencing data sets from Voigt (Voigt et al., 2019) and Cowan (Cowan et al., 2020) were downloaded as count matrices from Gene Expression Omnibus with the accession number GSE130636 or from https://data.iob.ch/, respectively. We used a standard pipeline relying on the Seurat (Hao et al., 2021; Stuart et al., 2019) package including normalization, scaling, identification of variable genes, dimensionality reduction, and cluster annotation based on known marker genes in line with the original studies. To mimic our proteomics approach, we then used the *FindMarkers* function to identify genes, that were specifically enriched (log2 fold change >0, adjusted p-value <.05) in the Müller cell clusters compared to retinal neurons including rods and cones as well as bipolar, amacrine,

horizontal, and ganglion cells. In the next step, we split the RMG clusters by region and performed differential gene expression analysis on the subclusters using the same function. For better comparison, we calculated the central to peripheral Müller cell expression ratio for each individual gene/protein and plotted the overlapping ones against each other in a scatter plot.

Quantification of morphological features as well as filopodia characteristics was performed with the CellProfiler (Jones et al., 2008; McQuin et al., 2018) software on the basis of actin staining of sparsely seeded cells across three independent experiments. First, individual cells were identified as primary objects, which were subsequently eroded to remove minor processes and filopodia and thus get the main cell body. The primary objects were then masked with the eroded objects and subsequently skeletonized to generate the outlines of cells without the body. Using the *MeasureObject* modules we quantified the branch parameters of the skeletonized outline for filopodia characterization and several other parameters of the primary objects representing the whole cells. The number of branch ends per cell was normalized to its perimeter as well as to the median number of detected branch ends per experiment to account for cell size and slight variation in contrast/image quality between experiments. The total branch lengths of a cell were additionally normalized to the number of its branch ends to get a measure of average filopodia length per cell.

Using CellProfiler, CD9 intensity was measured in three independent experiments by first identifying individual nuclei via DAPI staining as primary objects and the CD9 immunofluorescence as secondary objects around the nuclei. Intensity values per cell were normalized to median intensities per experiment.

We used the CytoScape (Shannon et al., 2003) software to create and explore gene/protein networks and perform pathway enrichment analysis via the StringApp plugin (Doncheva et al., 2019). Analysis scripts as well as CellProfiler pipelines are available upon request.

3 | RESULTS

3.1 | All-cone mice show generally healthy retinal layering with minor abnormalities in the outer retina

Grimm and colleagues described the generation and characterization of the R91W/Nrl$^{-/-}$ (from here on just "all-cone") mouse retina among others, in terms of structure, visual acuity and photoreceptor degeneration over time (Samardzija et al., 2014). To gauge its use as a model for the human macula, we wanted to test for possible differences between the all-cone retinal cytoarchitecture and its respective control carrying only the R91W mutation (from here on regarded as "control" in comparisons with all-cone samples). For this, we stained for cell type-specific markers, quantified the nuclei in the nuclear, and measured the thicknesses of the plexiform layers (Figure 1). Immunofluorescence staining for calretinin, a marker of inner retinal neurons including amacrine and ganglion cells, showed no significant difference between genotypes (Figure 1a,b), but the outer nuclear layer
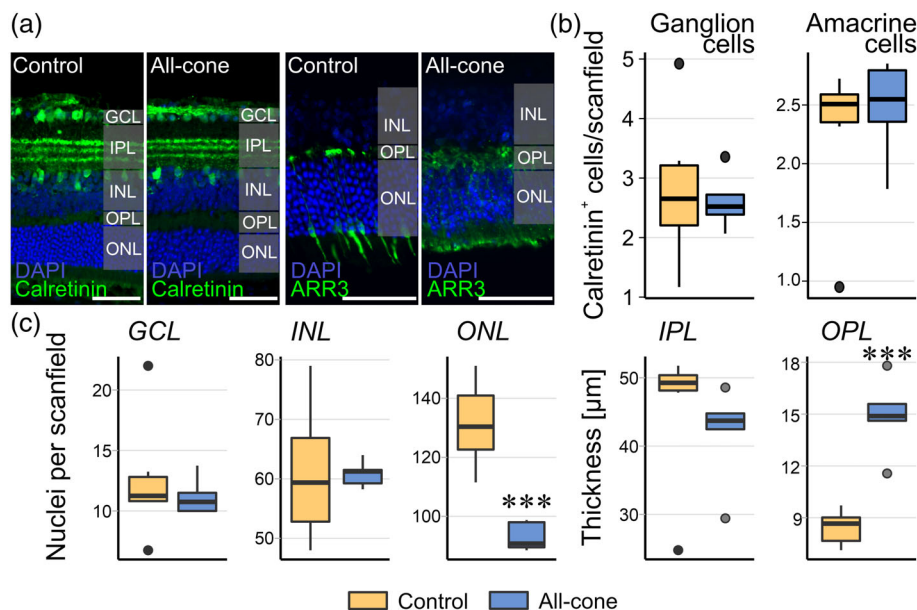
FIGURE 1 Morphological characterization of the all-cone mouse model. (a) Representative central retinal sections from control (R91W) and all-cone mice (R91W/Nrl$^{-/-}$). Cells of the inner retina were visualized by staining with calretinin, a ganglion and amacrine cell marker (left), while cones were delineated by staining for cone arrestin (ARR3, right). Scale bars, 50 μm. (b) Quantification of calretinin-positive cells in the ganglion cell layer (GCL) that comprise primarily ganglion cells and some displaced amacrine cells and in the inner nuclear layer (INL) representing amacrine cells. (c) DAPI-positive nuclei were quantified in all three retinal nuclear layers. We found on average 30% less nuclei in the outer nuclear layer of all-cone mice, while there were no differences in the other layers. Additionally, all-cone mice showed an almost twofold thicker outer plexiform layer than the control. (b, c) Box plots represent data from $n = 6$ control and $n = 5$ all-cone animals, respectively. Compared with control: ***$p < .001$; ONL, outer nuclear layer; OPL, outer plexiform layer; IPL, inner plexiform layer

(ONL) of the all-cone mouse contained ∼30% fewer cells (Figure 1c). Finally, we observed a significantly thicker outer plexiform layer (OPL) in the all-cone mice (Figure 1c). Cone arrestin (ARR3) staining in control mice showed the characteristic pattern of interspersed cone photoreceptors in the ONL ranging from synaptic terminals in the OPL to the outer segments thereby visualizing complete individual cells (Figure 1a). Individual cones were barely visible in the ONL of the all-cone mice, because of them being very densely packed, similar to what is observed in the human fovea. Additionally, we noticed abnormal outer segment morphology and rather disorganized cone pedicles in the OPL.

3.2 | Proteome profiling identifies differentially expressed proteins between cone- and rod- associated murine Müller cells

To enable the specific investigation of the Müller cell protein expression pattern from cone- or rod-rich mouse retina, we performed magnetic activated cell sorting (MACS) (Grosche et al., 2016; Pauly et al., 2019). This process of sequential cell depletion resulted in four cell populations—microglia (CD11b^{+}), endothelial cells (CD31^{+}), Müller cells (CD29^{+}), and neurons (CD11b^{-}, CD31^{-}, CD29^{-}). We confirmed the composition of the Müller cell fraction (CD29^{+}) in comparison to the neuron-enriched flowthrough by staining drop samples for the Müller cell marker glutamine synthetase (GLUL) and found

comparable enrichment as published earlier (Grosche et al., 2016). Not only were Müller cells present in a high percentage of more than 70% in the CD29 fraction, but also there was an almost complete absence of glutamine synthetase (GLUL)-positive cells in the flow-through, corroborating the good performance of the technique (Figure 2a). Importantly, the native elongated and arborized morphology of Müller cells was structurally preserved after the sorting (Figure 2a).

Tandem mass spectrometry was used to generate a complex proteomic data set with a total of ∼6000 identified proteins. The expression pattern of known marker genes confirmed the predominant cell types in the respective sorting fractions (Figure 2b). While Müller cell markers GLUL, RDH10 (retinol dehydrogenase 10), and RLBP1 (retinaldehyde-binding protein 1) were highly enriched in the CD29^{+} fractions of all samples, the CD11b^{-} fractions showed the highest expression of the microglial marker allograft inflammatory factor 1 (AIF1 alias IBA1), while CLDN5 (claudin 5) was most strongly expressed in the endothelial-rich CD31 (alias PECAM1—platelet and endothelial cell adhesion molecule 1)-positive fractions (Figure 2b). The triple-negative flowthrough, depleted from microglia, vascular cells and Müller cells had the highest expression in neuronal markers, especially cone arrestin (ARR3) (Figure 2b), confirming that this fraction mostly consisted of photoreceptors and retinal neurons. As expected, there was a significant difference in the expression of ARR3 between control and all-cone mice, corroborating their distinct photoreceptor identity (rod- vs. cone-dominated composition) (Figure 2b).

Principal component analysis (PCA) revealed clear clustering by cell type. In addition, Müller cells and neuronal fractions showed a moderate subclustering also by genotype, while CD11b and CD31 samples from control and all-cone mice seemed to intermingle (Figure 2c).

Because we were primarily interested in Müller cells and their interactions with photoreceptors, we focused further analyses on the proteins that showed Müller cell-specific expression in both genotypes, a total of 1929 proteins. Identification of differentially expressed proteins

(DEPs) was performed using the *limma* package in R (Ritchie et al., 2015). We detected 253 DEPs with an adjusted *p*-value lower than .05, of which 209 (54 with a fold change greater 2) were higher and 44 (18 with a fold change greater 2) lower expressed in cone only mice (Figure 2d–f; Table S2). Particularly EPPK1 (epiplakin) caught our interest, because it showed one of the highest expression differences in our mouse model (log2 fold change all-cone vs. control: 3.15, (Figure 2f)) while nothing is known about its function in the retina.
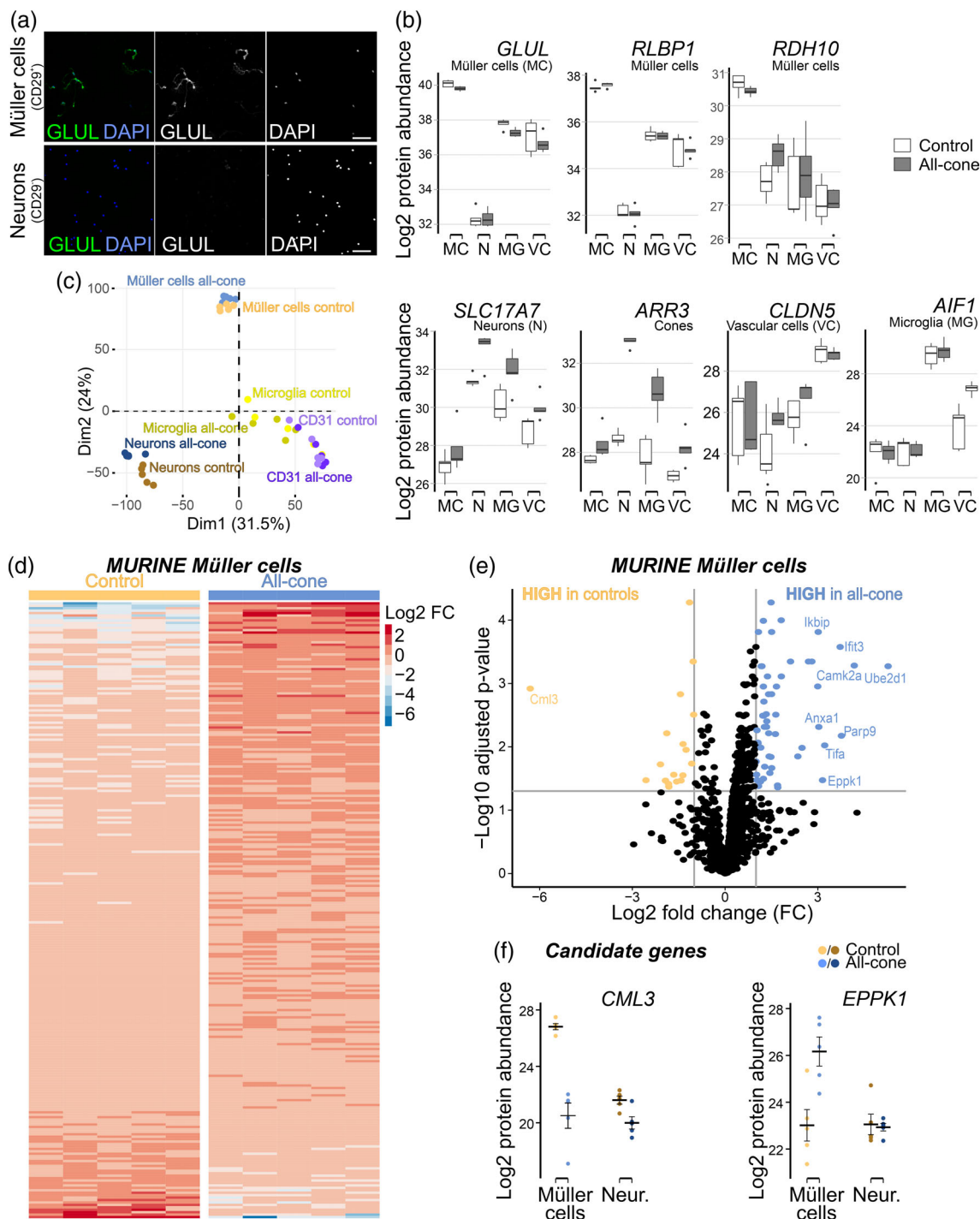

FIGURE 2 Legend on next page.

3.3 | Proteomic analysis identifies differentially expressed proteins between macular and peripheral human Müller cells

To compare differentially expressed proteins identified in the all-cone mouse model, we generated a comprehensive proteomic data set from Müller cells of the human macula (cone-rich) and periphery (rod-dominant). We collected postmortem retinal punches (6 mm in diameter) from the macula and periphery from 5 individual donor eyes (Figure S1), followed by MACS-based Müller cell isolation. As described for the mouse data set, we validated the purity of Müller cells and the photoreceptor-rich flowthrough by checking marker protein expression as determined by immunostaining and tandem mass spectrometry (Figure 3a,b). Müller cell markers GLUL, RDH10, and RLBP1 were enriched in the CD29-positive fraction, while ARR3, RHO, and PDE6G had the highest expression in the flowthrough (CD11b⁻, CD31⁻, and CD29⁻) (Figure 3b). Samples were clearly separated by cell type/fraction in the PCA, with the central and peripheral Müller cell fractions clearly segregated, whereas the neuronal fractions isolated from respective retinal areas showed some overlap (Figure 3c).

Analysis via the *limma* package identified 81 proteins with higher and 136 with lower expression in macular Müller cells compared to peripheral ones (Table S3). Notably, we found that only six proteins (S100A11, TTC39B, GLIPR2, BICD2, APOE, LMNA) were consistently and significantly enriched both in human macular as well as in all-cone mice Müller cells. Two proteins (ENO1, DHRS3) showed congruent downregulation in human and mice and also vimentin, a classical Müller cell marker, showed a slightly lower expression in macular Müller cells (Figures 3e, S3A) which we were able to corroborate by immunostaining (Figure S3B). Apart from those, novel interesting human-specific candidate proteins could be identified. For example 11-beta-hydroxysteroid dehydrogenase 1 (HSD11B1), an enzyme involved in glucocorticoid metabolism was expressed at significantly

higher levels in the macular Müller cell subpopulation (Figure 3f). In the context of glucocorticoid signaling in diabetic retinopathy (Ghaseminejad et al., 2020), it might be interesting to follow up in future studies. EPPK1, even though not reaching significance in this data set as in cone-rich mouse retina, was among the proteins expressed at higher levels in macular Müller cells (Figure 3f).

The list of these 217 differentially expressed proteins (DEP) was subjected to evaluation using the STRING database in combination with the CytoScape network analysis tool to identify functional connections between candidate genes. This resulted in a network encompassing 133 proteins, while 84 proteins were disconnected. Gene set enrichment analysis of the whole network revealed the highest enrichment in pathways related to extracellular exosomes and the basement membrane for a majority of the proteins including up- and downregulated ones (Figure 3g). Other enriched pathways included proteins involved in adhesion to the extracellular matrix (ECM) like various integrins, collagens as well as focal adhesion proteins TLN1 (Talin-1) and TNS1 (Tensin-1), which were all upregulated in macular Müller cells. Furthermore, proteins involved in the biosynthesis and/or transport of retinoid species RDH10, RLBP1, RBP1 (Retinol-binding protein 1) and DHRS3 (Short-chain dehydrogenase/reductase 3) were downregulated in the macula, while another member, RDH11, showed the trend of an inverse expression pattern (Figure S3A). We validated the findings for RDH10 of our proteomic screen via immunostaining of human retinal sections and showed a Müller cell-specific localization with a noticeably higher expression in peripheral regions (Figure S3B).

Recent advances in scRNAseq led to a growing number of publications studying tens of thousands of single cells from a variety of tissues including human retina. Our next question was whether the Müller cell heterogeneity suggested by our proteomic data was also reflected at the RNA level. We therefore explored publicly available resource data from Voigt et al. (2019) and Cowan et al. (2020) that profiled human retinal cells and compared them with respect to

FIGURE 2 Proteomic profiling of Müller cells isolated from rod- or cone-dominant murine retinae. (a) Sequential magnetic-activated cell sorting (MACS) based enrichment from all-cone and control (not shown) retinae yielded CD29⁺ cell fractions (top) that consisted almost exclusively of glutamine synthetase (GLUL)-positive cells with distinct morphology confirming their Müller cell identity. Flowthrough (CD11b⁻, CD31⁻, CD29⁻, bottom) was completely free of GLUL immunostaining thus consisting mostly of retinal neurons. Typically, ∼300.000 Müller glia are isolated from two pooled retinae of each mouse and ∼ 10 times more neurons. Scale bar, 50 μm. (b) Label-free mass spectrometric analysis shows that Müller cell markers GLUL, RLBP1 (retinaldehyde-binding protein 1) and retinol dehydrogenase 10 (RDH10) are highly expressed in the CD29⁺ retinal Müller cells (MC), while cone arrestin (ARR3) and vesicular glutamate transporter 1 (SLC17A7) are enriched in the triple-negative flowthrough, indicating that neurons (N) are the most abundant cell type here. AIF1 (allograft inflammatory factor 1 alias Iba1) and CLDN5 (Claudin-5) expression are highest in the CD11b⁺ and CD31⁺ fractions, respectively, thereby confirming their microglial (MG) and vascular cell (VC) composition. (c) Proteome profiling via mass spectrometry performed on the four cell fractions separated by MACS. Principal component analysis (PCA) shows a clear clustering of the samples primarily by cell type and especially for Müller cells and neurons also by genotype. (d) Heat map of 1929 Müller cell-specific, differentially expressed proteins identified by label-free tandem mass spectrometry. Limma identified 209 up- and 44 downregulated proteins in the all-cone mouse as compared to controls. Each vertical lane represents data from cells isolated from one individual animal (n = 5). (e) The volcano plot shows proteins that are significantly differentially expressed (adj. p-value <.05) between the genotypes. Blue: Upregulated >twofold in all-cone mice, yellow: Upregulated >twofold in control. proteins that show at least eight-fold upregulation are indicated by labels. (f) CML3 (N-acetyltransferase family 8 member 3, Nat8f3) expression as determined by mass spectrometric profiling is around 80-fold higher in control animals than in the double mutants, while EPPK1 is increased by more than eight-fold in cone-dominant retina error bars indicate mean plus standard error. Neur., neurons. (b–f) Label-free mass spectrometric analysis was performed on cell poplulations purified from retinae of 5 control and 5 all-cone mice, respectively

regional differences in the fovea and retinal periphery. We first identified genes that were enriched in Müller cells compared to neurons including cones, rods, bipolar, amacrine, and ganglion cells. The resulting genes were then subjected to differential expression analysis by comparing Müller cells of foveal/macular origin with their peripheral counterparts resulting in 477 and 742 differentially expressed
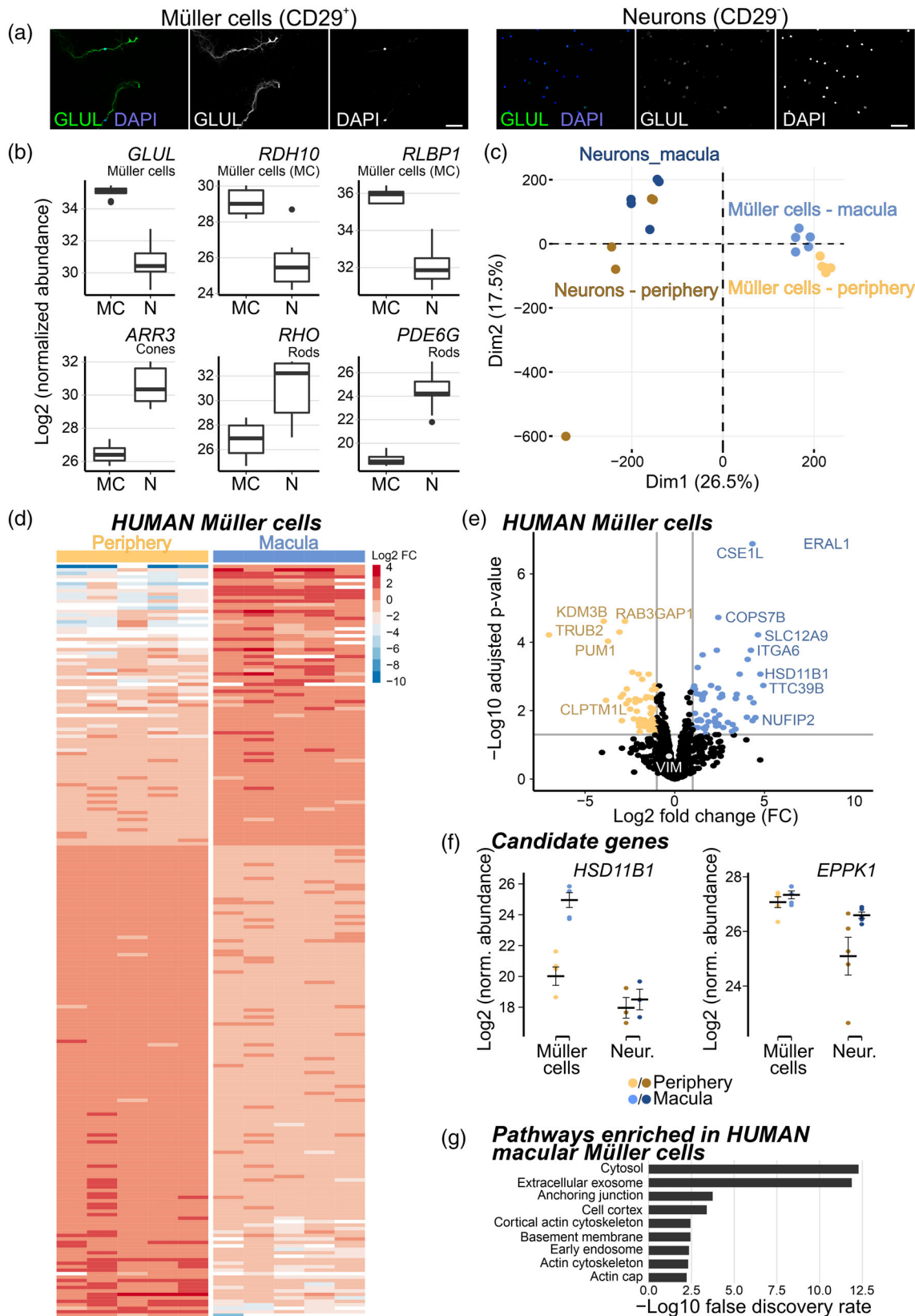

FIGURE 3   Legend on next page.

genes for the Voigt and Cowan studies, respectively. 33 and 68 of them, respectively, were also detected in our proteomic analysis, of which, importantly, the absolute majority (30 and 67, respectively) showed the same regionally distinct expression pattern (Figure 4a). Finally, a total of 29 genes with a congruent expression profile (11 up-, 18 downregulated in macula), were identified in all three data sets (Figure 4b).

Transcripts for EPPK1, our candidate with consistent expression profiles in human and mouse Müller cell proteomes, were identified only in Voigt et al. (2019). Because some transcripts were also detected in ganglion cells, they did not meet the above criteria for cross-validation of proteomes across scRNAseq data sets. However, a consistent trend toward higher EPPK1 transcript levels was observed in macular Müller cells compared with their peripheral counterparts (Figure S4).

3.4 | EPPK1 is specifically enriched in cone-associated Müller cells

Our study revealed high expression of EPPK1 protein in both mouse and human Müller cells (Figures 2 and 3). EPPK1, with a mass of around 500–700 kDa is a huge protein belonging to a family of cytoskeletal linkers like desmoplakin or plectin (Hu et al., 2018; Sonnenberg & Liem, 2007) and was shown to have domains that are capable to directly interact with intermediate filaments in hepatocytes or keratinocytes (Jang et al., 2005; Spazierer et al., 2008; Szabo et al., 2015; Wang et al., 2006). We found a similar EPPK1 expression pattern in humans and mice being specific to Müller cells and expressed stronger in glia isolated from cone-rich retina (Figure 2f, Figure 3f). While the interregional difference of EPPK1 protein expression was close to, but did not reach statistical significance in our human data set (one-tailed paired t-test p-value: 0.09), immunostaining on cryosections of human retina delineated a clear regional difference in the EPPK1 staining pattern, confirming its localization in macular Müller cells (Figure 5a). In line with this finding, the EPPK1 staining was confined to Müller cell inner and outer stem processes in all-cone and control mice with a beads-on-a-string to fibrillar appearance (Figure 5a). The higher staining intensity for EPPK1 in Müller cells from all-cone mice is consistent with our findings from mass spectrometric analysis (Figure 5a). Moreover, Western blot analysis done on retinal extracts from control and all-cone mice provided additional proof that EPPK1 levels are higher in cone-rich retina (Figure 5b). Co-blotting of retinal samples from wild type and *Eppk1* knockout (*Eppk1*$^{-/-}$) mice demonstrated specificity of the antibody, as no specific signal was detected in EPPK1-deficient retina (Figure 5b).

To assess whether EPPK1 is mandatory for retinal integrity, we studied the retinal architecture in *Eppk1*$^{-/-}$ mice. Notably, previous work showed that a knockout of *Eppk1* in mice did not lead to major phenotypic differences, even in tissues with high EPPK1 physiological expression levels, such as the skin (Goto et al., 2006; Spazierer et al., 2006), or to a disturbed keratin organization. A knockout in keratin 8, a close interaction partner of EPPK1, on the other hand, completely abolished the EPPK1 localization to the cellular periphery of wild-type hepatocytes demonstrating the dependence of a proper subcellular EPPK1 localization on keratin intermediate filaments (Szabo et al., 2015). Similarly, no obvious disturbance in retinal or Müller cell morphology was found in *Eppk1*$^{-/-}$ mice (Figure 5c), nor did we detect a disorganization in vimentin (VIM), another intermediate filament, which is specifically expressed in Müller cells but is, in contrast to GFAP, detectable at high levels already in Müller cells of the healthy retina. Next, we analyzed the EPPK1 localization in *Gfap/Vim* double knockout mice. The long EPPK1-positive beads-on-a-string-like structures seen in the wild type (Figure 5d) were absent, but shorter structures and a slight accumulation in the Müller cell somata could be detected.

Studies in liver (Szabo et al., 2015) and pancreas (Wögenstein et al., 2014) suggest a role in the organization of the intermediate filament network in response to pathological tissue alterations. In

FIGURE 3 Proteomic profiling of rod- or cone-associated human Müller cells. (a) Punches of 6 mm in diameter were dissected from macular and peripheral regions of retinal tissue from human donors and subsequently subjected to MACS sorting as described for mouse. CD29$^+$ fractions consisted almost entirely of glutamine synthetase (GLUL)-positive Müller cells that retained their intricate, elongated morphology, while cells of the flowthrough showed no staining for GLUL. Approximately 200.000 Müller glia are isolated from each 6 mm tissue punch and ∼ 3–4 times more neurons. Scale bar, 50 μm. (b) Neuronal (N)- and Müller cell (MC)-enriched cell fractions were analyzed using tandem mass spectrometry. Expression of retinal Müller glia markers GLUL, RDH10 and RLBP1 was found primarily in the CD29$^+$ fractions, while cone-arrestin (ARR3), rhodopsin (RHO) and phosphodiesterase 6G (PDE6G) were enriched in the flowthrough, representative of high photoreceptor content of the neuronal cell population. (c) Protein expression profiles determined by tandem mass spectrometry were separated mainly by cell type in a PCA. Furthermore, Müller cells grouped into tight subclusters according to their region of origin, whereas the intraregional difference between neuronal fractions appeared less pronounced. (d) Heat map of differentially expressed proteins determined by limma analysis of the proteome profiles of Müller cell subpopulations. Each vertical lane represents data from one donor eye ($n = 5$). (e) A volcano plot shows proteins with at least twofold upregulation in Müller cells of the macula (63, blue) or periphery (67, yellow), respectively. Labels for proteins with a fold change higher than 8 and an adjusted p-value <.01 are provided. (f) Corticosteroid 11-beta-dehydrogenase isozyme 1 (HSD11B1) is specifically enriched in Müller cells in both regions with a 30-fold higher expression in Müller cells of the macula. EPPK1, while being significantly upregulated in all-cone versus control mice, shows a similar tendency in human, but does not reach significance (one-sided, paired t test: p-value = .09). Error bars indicate mean ± standard error. Neur., neurons. (g) Pathway enrichment analysis on differentially regulated proteins from macular and peripheral human Müller cells presenting significantly enriched GO-term of cellular components. (b–f) Label-free mass spectrometric analysis was performed on cell populations purified from macular and peripheral retinal punches from five donor eyes
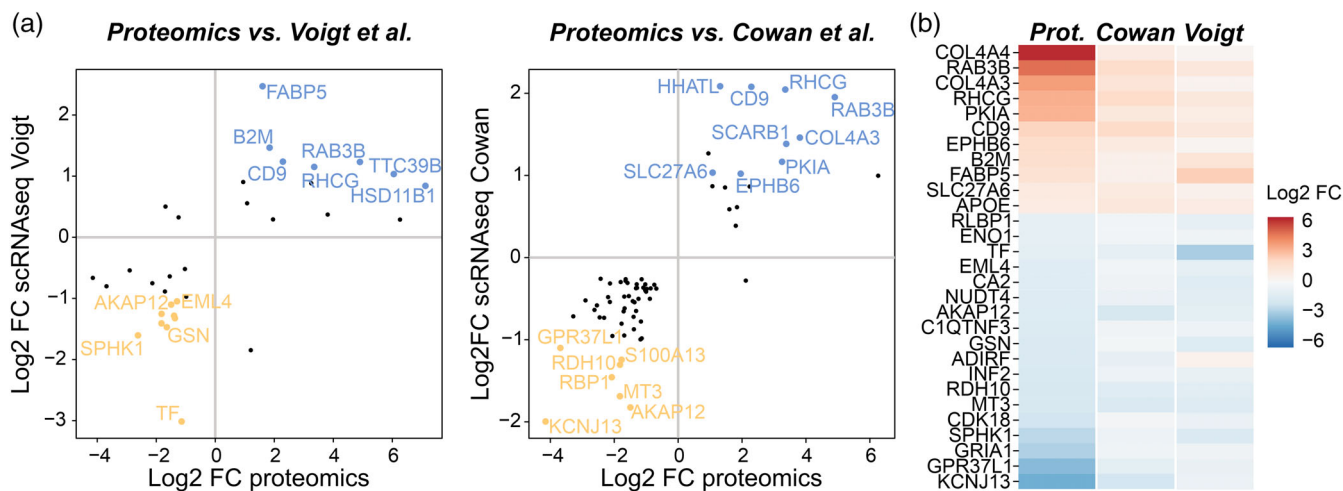
FIGURE 4 Comparison of human proteomic candidate genes identified as differentially expressed in Müller cell subpopulations with published human retinal scRNAseq datasets representing central (macula/fovea) and peripheral human retina. (a) From publicly available single-cell transcriptomic data sets generated by Voigt et al. as well as Cowan et al. (Cowan et al., 2020; Voigt et al., 2019) we identified genes that were specifically expressed in Müller cell clusters and showed significant difference between central and peripheral cells. Comparison of these differentially expressed genes with the proteomic data of the current study showed some degree of overlap with 33 genes from Voigt and 68 from Cowan being detected in both approaches. Genes/proteins that show a fold change (FC) of at least two on protein as well as on transcript level are colored, with blue indicating upregulation in macula and yellow upregulation in periphery. Most of the genes/proteins that were found to be differentially expressed in two methods also showed to be regulated in the same regional pattern. (b) Heat map showing a total of 29 genes/proteins differentially expressed in Müller cells (macula vs. peripheral region) that are shared among the three data sets

hepatocytes, keratin 8 is upregulated in parallel with EPPK1 (Szabo et al., 2015). In a similar fashion, one of the main intermediate filaments of Müller glia, GFAP, is upregulated during stress-induced gliosis such as transient retinal ischemia (Pannicke et al., 2018; Wunderlich et al., 2015). Accordingly, we examined EPPK1 localization in postischemic retinas exhibiting high GFAP expression in Müller cells, a model established by our group in another study (Mages et al., 2019). Indeed, we observed a more intense EPPK1 staining of gliotic Müller cells (Figure 5e,f) and super-resolution microscopy revealed a spot-like EPPK1 co-localization with GFAP filaments in the inner Müller glia stem processes (Figure 5e).

In sum, the concordant findings on the expression of EPPK1 in mouse and human retina make it a very interesting candidate that we have identified in our cross-species proteomic approach.

3.5 | EPPK1 knockout leads to morphological and biophysical changes of the human immortalized MIO-M1 Müller cell line

To date, the functional role of EPPK1 in glial cells or the retina in general has not been studied. Consequently, we sought to investigate EPPK1 function and its role in the central human retina. Due to the scarcity of human donor samples and the poor performance of primary Müller cells in vitro in regard to proliferation, morphological stability and accessibility for genetic manipulation, we chose the immortalized human MIO-M1 cell line (Limb et al., 2002) to start functional studies of EPPK1 in glia cells. Real-time quantitative PCR

(qPCR) analysis of RNA isolated from MIO-M1 cells and human donor retina revealed the presence of *EPPK1* mRNA in MIO-M1 cells, albeit at significantly lower levels than in human retinal extracts (Figure 6a). Consistent with this, EPPK1 protein was also identified by tandem mass spectrometry analysis of cell lysates from MIO-M1. (Figure 6b).

Next, we designed a CRISPR/Cas9-based genetic knockout (KO) approach to delete *EPPK1* for subsequent functional analysis. Peculiarly, despite its huge size of more than 20,000 bp, the genetic locus of *EPPK1* contains only two exons of which only the second is translated into protein. We defined a region of 1000 bps, starting with an annotated keratin binding site at the beginning of exon 2, to be targeted by our knockout strategy employing 4 guide RNAs (Figure 6c). The latter were designed to assure deletions stretching several dozens or hundreds of base pairs and thus ensuring either the generation of a premature stop codon or the creation of a truncated non-functional protein. After selection of puromycin-resistant transfected cells, two monoclonal colonies were chosen for further expansion.

Genotyping by PCR confirmed that these two cell lines, named C9 and F7, carried a deletion in their *EPPK1* gene (Figure 6d). Both showed a heterozygous genotype with one smaller (~500 bp) and one larger band (~1000 bp). The absence of a wild type band confirmed the absence of wild type cells in the monoclonal cultures. Sequencing of the two longer mutant DNA fragments revealed precise combined cuts of gRNA3 and gRNA1 that resulted in a deletion of 199 bp followed by a premature stop codon at amino acid position 143. The shorter mutant bands were the result of cuts by gRNAs 3 and 4 that resulted in an excision of 678 bp and a premature stop codon at amino acid 127. Lack of EPPK1 expression in C9 and F7 cell lines was
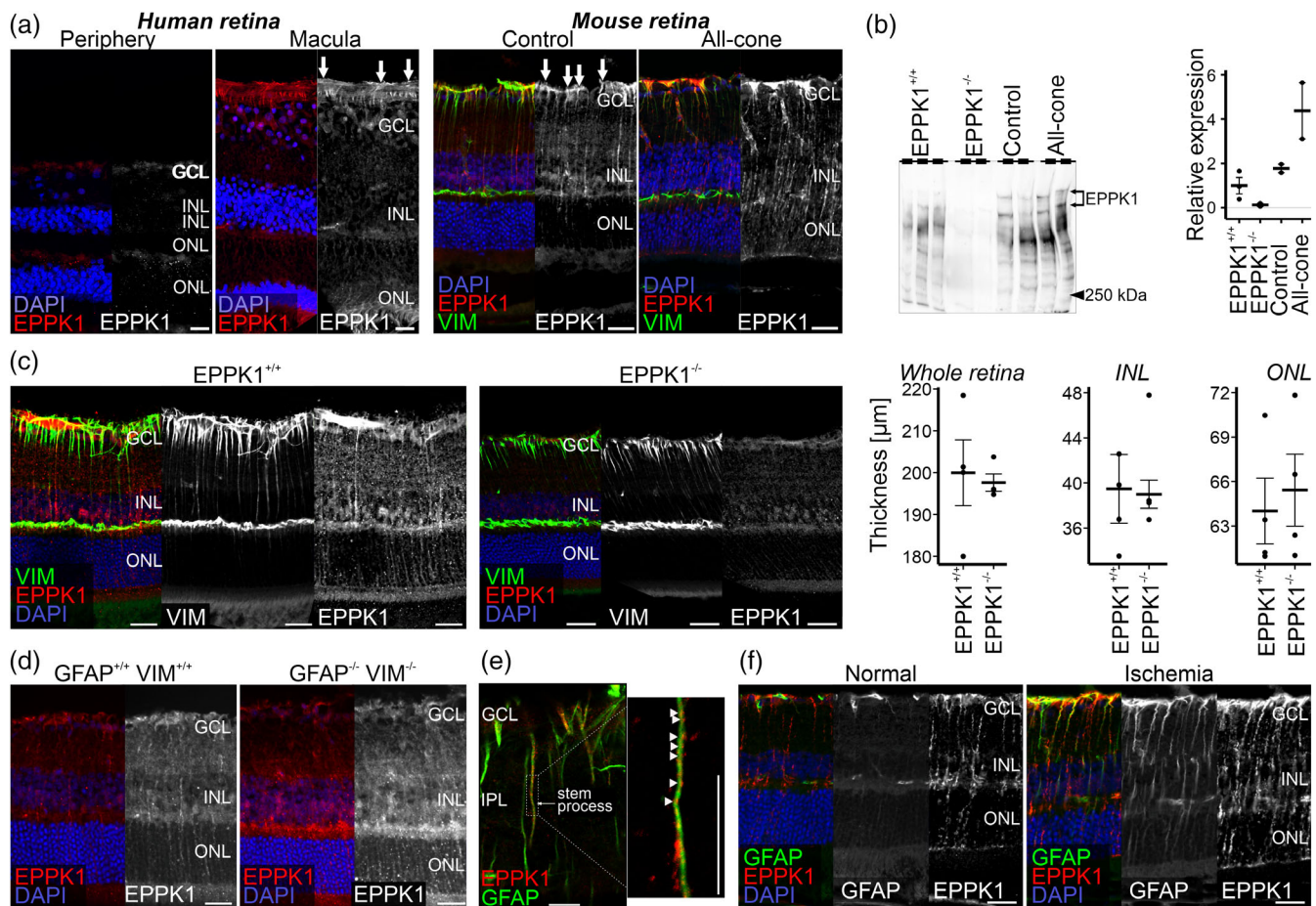
FIGURE 5 EPPK1 expression and localization in human retina and various genetic mouse models. (a) Immunostaining of EPPK1 in human retina showed signal in macular Müller cells, primarily in their endfeet (arrows), while such staining was almost completely absent in the periphery. A comparable staining pattern was observed in mouse retina, where EPPK1 also has a specific localization in Müller cells extending from their basal endfeet (arrows) to their stem processes extending into the outer retina. Co-labeling of vimentin, a classical Müller cell marker, and EPPK1 in mouse retinal sections shows that EPPK1 is mainly localized in Müller cell processes. Scale bars, 50 μm. (b) The implemented anti-EPPK1 antibody shows protein specific binding in Western blot analysis with several bands in wild type due to protein degradation as frequently observed in protein lysates derived from mouse tissues. However, no immune-reactive bands were detected in samples from Eppk1 knockout (Eppk1$^{-/-}$) retina. Increased EPPK1 protein expression was confirmed for all-cone versus control retina. Quantification was performed on the upper two bands (arrows) showing molecular weights expected for intact mouse EPPK1 protein variants (Ueo et al., 2021). (c) Left, representative images of retinal sections stained for EPPK1 and the intermediate filament vimentin. Genetic Eppk1 ablation has no gross effect on the organization or localization of vimentin in Müller cells. Right, quantification of the thickness of the whole central retina or the respective layers shows comparable gross retinal architecture in Eppk1$^{-/-}$ retina compared to controls. Data is represented as mean and standard error from four individuals per group. (d) Immunostaining of EPPK1 in retinae lacking both main glial intermediate filaments GFAP and vimentin indicate a shift from a filamentous to a more disorganized EPPK1 localization associated with a displacement into the somata of Müller cells. Scale bars, 20 μm. (e) EPPK1 seemed to be upregulated in a retinal pathology model (transient ischemia) and can be seen to co-localize spot-like (arrowheads) with GFAP-positive Müller cell stem processes visualized by STED microscopy. Scale bar, 10 μm (f) high intraocular pressure led to reactive gliosis of Müller cells and thus to an upregulation of GFAP (right), while it is usually not detectable in healthy cells (left). GCL, ganglion cell layer; INL, inner nuclear layer; ONL, outer nuclear layer

confirmed by qPCR at transcript (Figure 6e) and by Western blot at protein level (Figure 6f).

We then used proteomic profiling to assess possible molecular perturbations of *EPPK1* knockout Müller cells and/or their secretome. We harvested the cell lysates and conditioned medium from mutant and wild type cells and performed tandem mass spectrometric analysis. Checking for the cell lysates first, we found a downregulation of cell adhesion and extracellular matrix proteins like collagens, aggrecan core protein, and fibronectin (Table S4), analogous to human peripheral Müller cells. Similarly, pathway enrichment analysis revealed a dysregulation of vesicle-related pathways (Figure 6g). Regarding the secretome, we observed a downregulation of extracellular matrix proteins like collagens, fibronectin, chondroitin sulfate proteins and other adhesion molecules (Table S5). Accordingly, pathway enrichment analysis clearly points toward a reduced secretion of components of the extracellular matrix via extracellular vesicles (Figure 6g).

Next, we characterized potential effects of the *EPPK1* knockout on cell morphology by staining the actin cytoskeleton using phalloidin (Figure 7a). We noticed a reduction in cell size as well as an increased number of fine filopodia (Figure 7a,b). The outlines of the cells were segmented using CellProfiler software and various parameters such as cell area, solidity, elongation, form factor, and others were quantified.
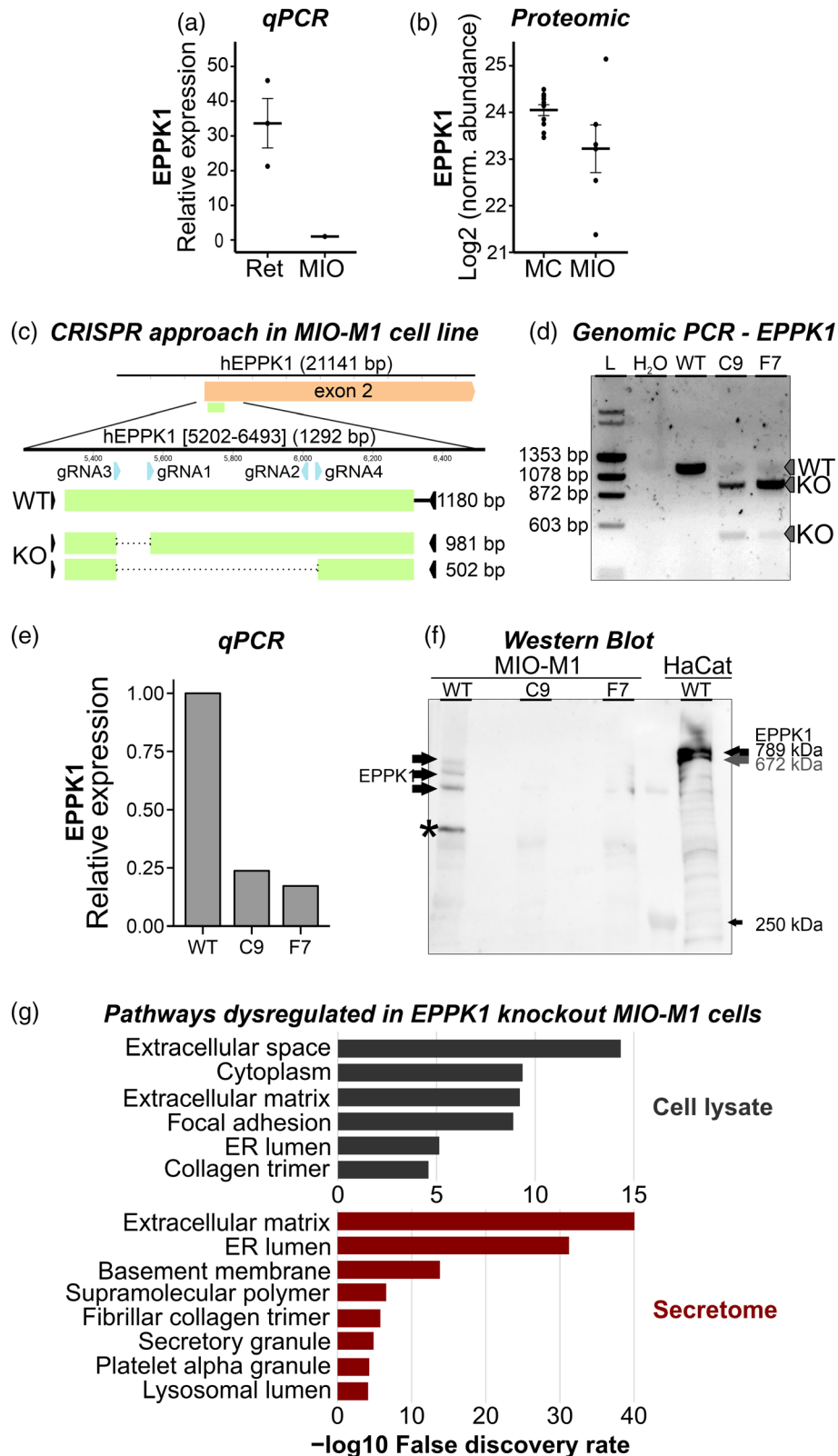

FIGURE 6 Legend on next page.

Most notably, we identified a significant and consistent decrease of the overall cell area in both knockout lines of around 35% (Figure 7b). Another prominent parameter was solidity, which is the ratio between the area of the cell and its convex hull which is spread out by its protrusions. It can thus be used as an indirect measure of the cell's morphology, e.g., their complexity, with values closer to 1 indicating roundish, regularly shaped cells and values closer to 0 indicating cells with many complex processes (Janssen et al., 2022; Lobo et al., 2016). Although we observed some variation in the shape of the cells of all genotypes, C9 and F7 exhibited a more regular morphology with fewer large projections. This was reflected in their significantly higher solidity (Figure 7b).

Additionally, through an image-processing pipeline that included segmentation, erosion, masking, and skeletonization, we were able to robustly segment filopodia of individual cells (Figure 7a). This allowed us to count the number of filopodia per cell and calculate their average length. EPPK1 knockout resulted in an increase in the number of filopodia with a simultaneous decrease in filopodia length (Figure 7c).

As cell morphology and filopodial dynamics are mainly regulated through the cytoskeleton, which also generates forces critical for cell function and retinal tissue integrity (MacDonald et al., 2015), we investigated the dependence of force generation by Müller cells on EPPK1 using traction force microscopy. For this, we grew cells on polyacrylamide substrates with a shear modulus of G' = 1000 Pa ($\sim$ 3000 Pa Young's modulus), which is in the range of reported moduli for retina (Ferrara et al., 2021), but which is much softer than tissue culture plastics (G' $\sim$ GPa) (Akhmanova et al., 2015) and found cells of various morphologies in both mutant cell lines and controls. While about half of the cells (49%–59%) displayed a spherical morphology and a smaller part (6%–27%) showed more arborized structure, we focused on bipolar cells (24%–34%) as shown in Figure 7d for our measurements. We analyzed the displacement of the embedded fluorescent beads after removal of the cells and subsequent relaxation of the gels to calculate the forces required for the initial deformation. The highest contractile forces were generated at the cell poles. EPPK1-deficient cells exerted significantly lower forces on their substrate than control cells, with a reduction of about 30% to 40% (Figure 7d).

Given the morphological and biomechanical changes in the absence of EPPK1 in MIO-M1 cells and the implication of exocytotic pathways (Figure 6g), we wanted to investigate whether knockout of EPPK1 affects extracellular vesicle transport. There is evidence that intracellular exosome trafficking requires interaction with intermediate filaments in glial cells (Margiotta & Bucci, 2016; Potokar et al., 2007). Interestingly, tetraspanin CD9, a common vesicle-associated protein (Escola et al., 1998; Théry et al., 1999; Théry et al., 2018), was specifically expressed by Müller cells and enriched in the Müller cell subpopulation of the macular region (Figure S3)—a pattern that was also consistent in two scRNAseq data sets (Figure 4b). Immunostaining of MIO-M1 knockout cells for CD9 revealed that EPPK1 knockout cells exhibited significantly lower staining intensity (Figure 7e). Proteomic analysis of knockout and wild type MIO-M1 cells corroborated these findings, showing that as in human peripheral Müller cells, indeed CD9 protein abundance is lower in EPPK1-ablated cells (Figure 7f).

Finally, we wondered whether the difference in intracellular CD9 expression depends primarily on a decreased protein synthesis or on a general shift in exocytosis. While we saw no difference in CD9 protein amounts in the secretome of EPPK1 knockout and WT (Table S5), nanoparticle tracking analysis of conditioned medium showed a decrease in the secretion of small extracellular vesicles (<200 nm) from both knockout cell lines, with C9 cells releasing about three times less particles into the medium than the control (Figure 7g).

4 | DISCUSSION

The human macula is a peculiar structure essential for sharp vision, but unfortunately, also very susceptible to diseases like age-related macular degeneration (AMD), diabetic macular edema or macular telangiectasia type 2 (MacTel2). To date, many studies have focused on the role of different retinal cell types like microglia (Altmann & Schmidt, 2018) or the vasculature (Yeo et al., 2019) in the macula in pathological as well as in healthy conditions. Although morphological and functional differences between macular and peripheral Müller glia were addressed in few studies (Syrbe et al., 2018; Wang &

FIGURE 6 Generation and validation of EPPK1-deficient MIO-M1 Müller cell lines. Comparison of EPPK1 expression between human donor retina and the immortalized human Müller cell derived cell line MIO-M1, shows that transcript (a) as well as protein (b) is detectable in the latter, albeit at a lower level than in native tissue. Error bars indicate mean ± standard error. (c) The human EPPK1 locus (top) consists of one small, untranslated and one huge, $\sim$16,000 bp long exon that encodes for the whole translated region. For CRISPR/Cas9 mediated knockout (KO), we designed guide RNAs to target a 1000 bp long region at the beginning of a predicted keratin binding site. To ensure complete knockout of the gene, we transfected the cells with a combination of four guide RNAs and generated two monoclonal cell lines, C9 and F7. (d) PCR amplification of the target region resulted in one band with the expected size of 1180 bp for wild type cells, while the mutant lines showed two bands each. Sequencing of the mutant PCR fragments revealed cuts by gRNA3, gRNA1, and gRNA3, gRNA4 leading to a deletion of 199 bp and 678 bp, respectively (c, bottom). Quantitative PCR ((e), mean of two technical replicates) and Western blot analysis (f) confirmed successful knockout of EPPK1 in the mutant cell lines. Wild type MIO-M1 cells showed three high molecular bands, maybe due to the triploidy of chromosome 8 (Limb et al., 2002), on which EPPK1 is encoded. a fourth band, visible in the wild type (asterisk), might be a degradation artifact. The HaCat wild-type cell line (keratinocyte origin) was used as a positive control showing two immune-reactive bands at the expected molecular weight (789 and 672 k Da, respectively). The respective EPPK1 knockout lines (C9, F7) lacked any immune-reactive bands. Size differences of EPPK1 may occur between samples originating from non-isogenic individuals (Ishikawa et al., 2018). (g) the plot shows GO terms (cellular components) for proteins found at different levels in cell lysate or the secretome of control and EPPK1-deficient MIO-M1 lines. ER, endoplasmic reticulum

Kefalov, 2009; Zhang et al., 2019), there is no deeper understanding of molecular protein pathways involved in regional Müller cell heterogeneity. In this study, we used multiple models in a multiomic approach to start closing this knowledge gap and to identify specific proteins that shape functional differences between central and peripheral Müller cells. Using the all-cone mice, we first studied differences between Müller glia in a cone-rich retina, compared to rod-rich

normal controls in order to characterize this aspect of regional differences in photoreceptor subtype distribution in the human macular and peripheral retina, respectively. It has been shown that all-cone mice are capable of functional vision and have normal retinal layering (Samardzija et al., 2014). Nevertheless, we performed additional in-depth characterization of the cellular composition as well as morphometric quantification of all retinal layers, in order to exclude possible
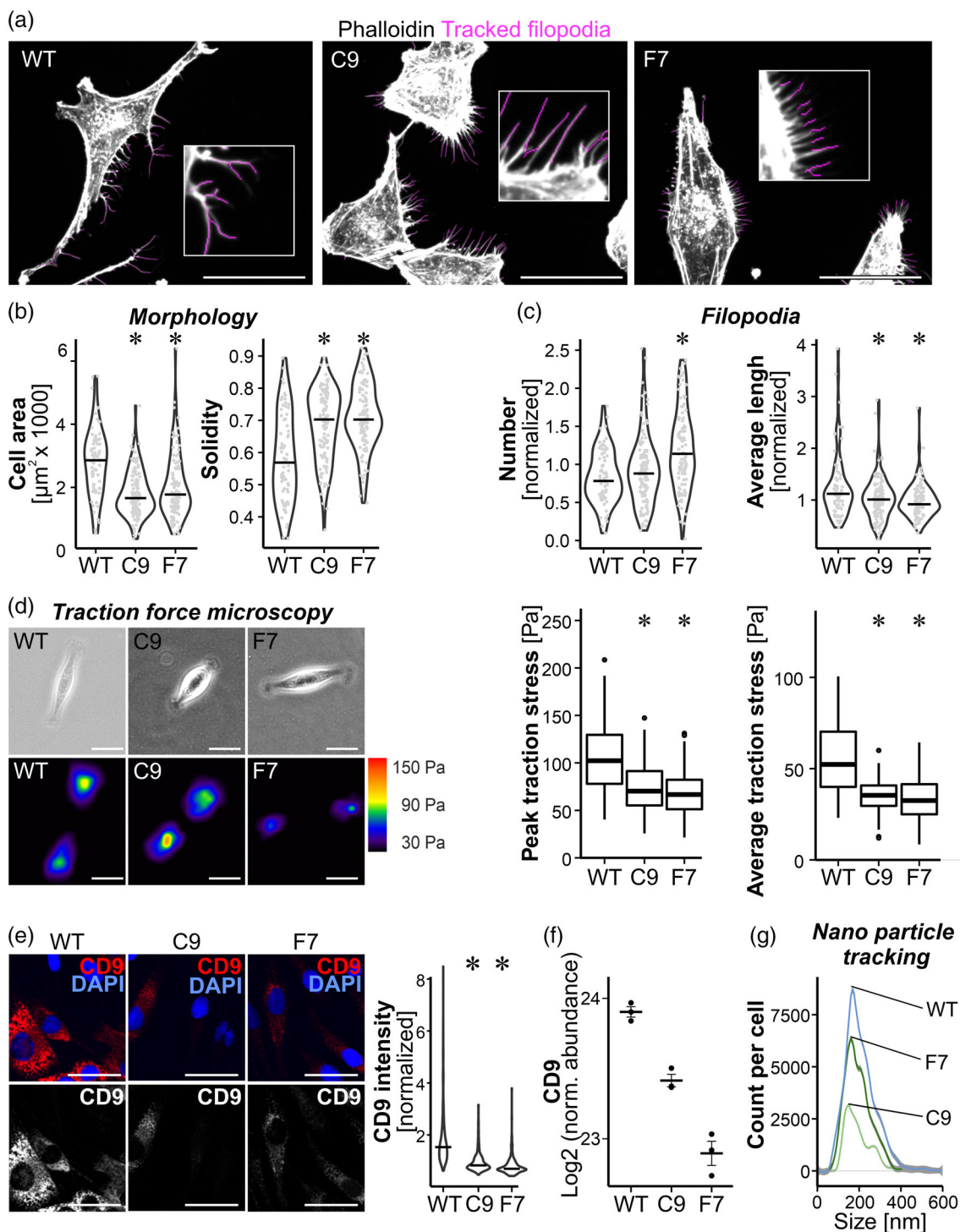

FIGURE 7 Legend on next page.

confounding factors from cone-independent retinal changes, like inner neuron composition. Complementary to the morphological analysis performed by Samardzija et al. (2014), we found minor alterations of the outer nuclear layer, with a lower number of nuclei in the all-cone retina. It is unclear whether this discrepancy develops during embryonal stages, maybe due to inefficient cone differentiation, or whether it is a sign of photoreceptor degeneration after birth as a result of the double mutation (Samardzija et al., 2014).

The increased thickness of the outer plexiform layer might be explained by cone pedicles, the synaptic structures relaying signals to the neurons of the inner nuclear layer, being bigger than the corresponding rod spherules (Hoon et al., 2014; Kolb, 1995; Wässle et al., 2002). Although the exact wiring and signal transduction remain elusive and require further studies on this model, we did not find any obvious changes of the inner retinal layers in terms of thickness and gross cellular composition.

Although the all-cone mouse retina may yield some insights regarding Müller cell-cone interaction, it does not reproduce key characteristics of the human macula like the pit-like morphology and avascular zone of the fovea, as well as a gradient of cone diversity and distribution. Still, we assessed whether at least some aspects of human cone-associated Müller cell heterogeneity could be modeled. Therefore, we examined the proteome of Müller cells from the macula and periphery of human donor retinas for comparison. Indeed, in our proteomic approach, we found only eight proteins to be significantly differentially expressed in both datasets. This suggests that although there does not seem to be a broad congruence between all-cone and macular Müller cells, there seems to be some core proteins important for Müller cell cone interaction like APOE (Apolipoprotein E), LMNA (Prelamin-A/C), ENO1 (Alpha-enolase) or DHRS3.

Comparing our proteome data with two published single cell RNAseq datasets, we found several differentially expressed genes consistently detected in both transcriptomic and proteomic profiles. Although there is increasing evidence that protein levels can be uncoupled from the synthesis of their transcript by a variety of mechanisms (Liu et al., 2016; Noya et al., 2019; Sharma et al., 2015;

Vogel & Marcotte, 2012), we found that genes that overlap in the datasets analyzed here were mostly regulated in the same manner—29 genes showed a consistent regulatory pattern across all three data sets. These included CD9, a member of the tetraspanin family involved in the biogenesis of extracellular vesicles, as well as RDH10 and RLBP1. Unexpectedly, RDH10, RLBP1, RBP1 and DHRS3, all bona fide proteins of the visual cycle, were higher expressed in peripheral Müller cells. This seems counterintuitive, as studies report that cones, which are present in exceptionally high number in the macular retina, specifically rely on the function of these Müller cell-specific genes/proteins for the regeneration of their photopigment (Kaylor et al., 2013; Wang & Kefalov, 2009; Xue et al., 2015). However, because there are no rods with long outer segments in the fovea to keep the RPE at a distance from the cones and also because the outer segments of the cones are exceptionally longer in the fovea (Domdei et al., 2021; Tschulakow et al., 2018; Yuodelis & Hendrickson, 1986) than in the peripheral retina, the RPE can potentially take care of the cones better in the fovea than in the periphery. Notably, DHRS3, an enzyme that opposes RDH10 in the synthesis of retinaldehyde (Adams et al., 2014; Belyaeva et al., 2019), was one of eight proteins consistently lower in cone-rich samples of both, human and mouse Müller cells. An ablation of Dhrs3 during development was shown to lead to an accumulation of all-trans retinoic acid (ATRA) with a concurrent reduction of the retinol pool resulting in embryonic lethality (Billings et al., 2013). The same study found a downregulation of Rdh10 in response to Dhrs3 knockout, leading the authors to hypothesize this to be a measure to counter increased ATRA levels. Since ATRA is a known transcriptional regulator involved in a multitude of gene regulatory networks (Balmer & Blomhoff, 2002; da Silva & Cepko, 2017; Kam et al., 2012; Thompson et al., 2019), it is crucial to tightly control its synthesis, which might be a major function of RDH10 and DHRS3 in Müller cells. In agreement with this, several knockout experiments in cones, Müller cells, and the whole retina have shown, that RDH10 is not required for proper cone function (Xue et al., 2017), leading to the assumption that other retinol dehydrogenase family proteins must be involved in the Müller cell-dependent

FIGURE 7 Morphological, molecular, and functional signature of the human Müller cell line MIO-M1 deficient for EPPK1. (a) MIO-M1 cells cultured on glass coverslips and stained with phalloidin to visualize actin filaments and thereby the general morphology including fine filopodia (insets). Using the CellProfiler image analysis software, we were able to quantify several cell morphological characteristics including filopodia length (highlighted in purple) and number. (b) Measurements of cell area as well as solidity, which can be seen as a proxy for cell branching with higher values meaning less cell processes, showed a significant decrease in cell size and complexity of both EPPK1 knockout (KO) lines C9 and F7. (c) EPPK1 knockout cells had significantly shorter, but more filopodia. The bar inside violin plots represents the median. (d) Wild type and knockout MIO-M1 cells were cultured on polyacrylamide gels with a shear modulus of 1000 Pa and embedded fluorescent beads. Comparing the positions of the beads between cell-associated and relaxed state (cells were removed), allowed the calculation of traction stress exerted by the cells. Polar cells of all lineages, wild type or EPPK1 knockout (top), imposed primarily traction forces on the gel at their poles, which pulled in the direction of their soma (bottom). Compared to wild types, EPPK1 knockout cells exerted weaker peak as well as average stress onto their gel substrate. n: Peak traction stress: C9 = 31, F7 = 38, WT = 33; average traction tress: C9 = 29, F7 = 38, WT = 33. (e) Left, staining of CD9 localized primarily around nuclei and showed a decreased signal in EPPK1 knockout cell lines C9 and F7. Right, intensity measurements of CD9 staining per nucleus confirms a significantly lower expression in mutant cells. The bar inside violin plots represents the median. (f) CD9 protein expression is significantly reduced in both EPPK1 knockout MIO-M1 lines as determined by mass spectrometric protein quantification. Error bars indicate mean ± standard error. (g) Nano particle tracking analysis (NTA) of medium supernatant collected from wild type as well as knockout cells (mean of two technical replicates) suggests a decrease in the secretion of extracellular vesicles by the C9 and F7 lines. (a, d, e) scale bars, 50 μm. (b, c, d, e) p < .05; compared with WT control

cone visual cycle. In this context, RDH11 would be an interesting candidate, since it has similar enzymatic activity (Belyaeva et al., 2019) and tends to be higher expressed in foveal Müller cells (Figure S3). Which isomerization and/or oxidation steps of the cone visual cycle actually occur in Müller cells and which proteins catalyze these reactions have not yet been completely elucidated, but the data provided in this study can serve as a starting point.

As pointed out before, hundreds of Müller cell-specific proteins were found to be differentially regulated. EPPK1 showed one of the highest expression differences in the all-cone mouse model. Immunofluorescence staining for EPPK1 confirmed its Müller cell-specific expression pattern as well as a beads-on–a-string-like co-localization with the glial intermediate filaments vimentin and GFAP. Previously, EPPK1 was shown to not only co-localize with a variety of keratins and vimentin, but also to be able to physically bind to them in in vitro studies (Jang et al., 2005; Spazierer et al., 2008; Szabo et al., 2015; Wang et al., 2006). The effect of EPPK1 deficiency in mice seems to be dependent on cell type and tissue health, with no obvious phenotype in normal epidermal and hepatic cells, whereas it leads to a disruption of intermediate filaments in HeLa cells and to impaired disease-induced keratin network reorganization in disease models of liver and pancreas (Jang et al., 2005; Spazierer et al., 2006; Szabo et al., 2015; Wögenstein et al., 2014). Likewise, we did neither find morphological defects in the retina of healthy *Eppk1* knockout mice nor in the vimentin network of their Müller cells. Since the ablation in this mouse line is of constitutive nature, it could be that EPPK1 deficiency is compensated either by other members of the plakin family or proteins similarly involved in the formation of cytoskeletal morphology and/or adhesion as has been suggested for envoplakin, periplakin, and keratins (Inaba et al., 2020; Tonoike et al., 2011). In *Gfap/Vim* double knockout retinae, we found a disruption of the filamentous structure of the EPPK1 staining pattern with a concurrent increased localization in Müller cell somata, suggesting that EPPK1 is not required for intermediate filament organization in wild-type retinae, whereas GFAP and/or vimentin appear to be required for proper EPPK1 localization. This finding is in line with an observation in keratin 8 knockout cells, where EPPK1 was completely delocalized, while there seemed to be no effect of *Eppk1* knockout on keratin 8 (Szabo et al., 2015). But what might this mean for primarily cone-associated Müller cells in the retina where EPPK1 showed an increased expression?

Although EPPK1 transcripts seem to be rare and are detected only at very low levels in Müller cells and to some extent also in ganglion cells in the scRNAseq datasets of human donor retinas (Voigt et al., 2019), we confirmed by immunostaining that the protein is specifically expressed in human Müller cells, whereas a low level of expression in ganglion cell axons cannot be completely excluded. Additionally, qPCR, mass spectrometry, and Western blot analysis showed EPPK1 expression in the human Müller glia derived cell line MIO-M1. In vivo, Müller cells are thought to confer mechanical stability to the retina (MacDonald et al., 2015). However, in the parafoveal region Müller cells in particular must meet special biomechanical requirements to maintain the structural integrity of the tissue because of at least two factors: (i) their elongated and z-shaped morphology resulting in large Müller cells and (ii) the potentially increased

mechanical strain, for example, employed by the vitreous body that is especially tightly attached to the macular retina (Syrbe et al., 2018). Moreover, it has even been speculated that Müller cells help maintain or even form the foveal pit (Bringmann et al., 2018, 2020). Here, we found evidence that EPPK1 might be involved in these functions, as its knockout in MIO-M1 cells led to (i) smaller cells with fewer protrusions and (ii) weaker traction forces. This, in turn, indicates that increased EPPK1 expression in macular Müller cells may contribute to the formation of their larger, more complex morphology as well as to the ability to exert the increased mechanical forces required to shape the fovea. In line with the discussed theory, we also found an increase in extracellular matrix proteins and adhesion molecules in macular Müller cells consistent with published scRNAseq datasets. Thus, it appears that Müller cells in the macula have not only enhanced expression of proteins like EPPK1 that seem to be key for the exertion of higher traction forces and cell-ECM interaction, but also ECM components themselves. Several collagens (COL4A1, COL4A3, COL4A4) and other ECM associated proteins (ITGA6 [Integrin alpha-6], LMNA) together with lipid binding proteins such as APOE and FABP5 (Fatty acid-binding protein 5) are highest expressed in macular Müller cells, suggesting a remodeling of the microenvironment in regard to intercellular transport of metabolites (Liu et al., 2017; Napoli, 2012), ECM composition and stiffness (Bachmann et al., 2019; Bourgot et al., 2020). Importantly, EPPK1 seems to be deeply embedded into this functional network as demonstrated by the perturbances of cell morphology and function of its knockout in the human Müller cell-derived cell line.

The massive downregulation of CD9 after *EPPK1* knockout might reveal another, perhaps indirect, function of EPPK1. CD9 is one of the proteins with the most consistent expression profiles at both the transcript and protein levels in human retina, with significantly higher expression (like EPPK1) in cone-associated Müller cells. Previously, intermediate filaments were associated with vesicular transport (Margiotta & Bucci, 2016; Potokar et al., 2007, 2020) and EPPK1 was shown to bind directly to several intermediate filaments, including vimentin (Jang et al., 2005; Wang et al., 2006). Therefore, EPPK1 might affect vesicle transport either directly, by promoting the binding of intermediate filaments and vesicles, or indirectly, by modifying the rigidity/density of the cytoskeletal meshwork. In contrast to the cell lysate, we did not find a difference in CD9 abundance in the secretome of EPPK1-ablated cells, but an overall decrease in the number of released small extracellular vesicles (EVs). We thus hypothesize that most vesicles shed from the Müller cell line carry CD9 making it an interesting candidate to follow up on mechanisms of Müller cell secretion, while CD9-dependent EV biogenesis seems EPPK1-independent. In contrast, intracellular trafficking of structures relevant for EV shedding were disrupted, as we observed less EVs in the supernatant. Together with the finding that proteins of the ECM (collagens, fibronectin, and chondroitin sulfate proteins) were highly abundant in the secretome of wild type cells, but significantly downregulated in both EPPK1-deficient MIO-M1 lines, this could imply that EPPK1 does not only confer mechanical stability to those huge z-shaped macular Müller cells, but also coordinates transport and release of proteins

across long distances in those Müller cells. The pronounced deposition of ECM components by Müller cells could be the central basis for the intense interaction with associated tissues or cells including the vitreous body especially in the macula. In line with this, there have even been reports of CD9 promoting cell–cell adhesion through direct interaction with other cell surface proteins like integrins (Reyes et al., 2018) or ICAM1 (Intercellular adhesion molecule 1) (Franz et al., 2016) in a vesicle-independent manner—an additional research strand that should be further pursued in future studies to understand the very specific biomechanical microenvironment of the human macula achieved by the cells located there.

Several studies suggested genes involved in serine biosynthesis like *PHGDH* (D-3-phosphoglycerate dehydrogenase) as well as glycolytic pathways to be risk factors for MacTel2 (Gantner et al., 2019; Scerri et al., 2017). Subsequently, Zhang et al. were able to show that the same proteins were indeed differentially expressed between Müller cells of foveal and peripheral origin already in a healthy state (Zhang et al., 2019). Looking at our data, we did not see any changes in PHGDH between macular and peripheral Müller cells. This discrepancy might stem from the different source material, being acutely and specifically isolated Müller cells in our case, and Müller cells growing out of retinal pieces after weeks in culture for Zhang et al. (2019), where massive metabolic changes can occur. Interestingly, another finding was the notably different morphology of cultured central and peripheral Müller cells and a subsequent differential expression of pathways related to extracellular matrix organization in line with our observations. In contrast to our findings, Zhang and colleagues noticed smaller cells with less complexity concomitant with an upregulation in ECM pathways in Müller cells of macular origin. The source of this discrepancy is unclear, but it is worthwhile following up for example in the context of macular holes emerging during MacTel2 disease (Heeren et al., 2020), which might not be explained with a difference in serine biosynthesis.

5 | CONCLUSION

Previous studies showed that the central human retina not only presents a microenvironment with specific characteristics that produces challenges to the inhabitant cells different to the periphery, but that it is also highly susceptible to debilitating diseases. Here, we focused on Müller cells and were able to uncover differentially regulated pathways mainly, but not exclusively, linked to secretory and cell adhesion systems. Furthermore, we identified EPPK1 and CD9 to be enriched in macular Müller cells, implicating a role in the cells' biophysical properties as well as intracellular vesicle trafficking and their release. Nevertheless, future studies need to clarify the exact mode of interaction between EPPK1 and CD9 and their potential role in macular pathological processes.

AUTHOR CONTRIBUTIONS

Conceptualization: Lew Kaplan, Peter Fuchs, Berta Puig, Kristian Franze, Stefanie M. Hauck, Antje Grosche. *Methodology*: Lew Kaplan, Corinne Drexler, Anna M. Pfaller, Santra Brenna, Kirsten A. Wunderlich, Andrea Dimitracopoulos, Maria-Theresa Perez, Ursula Schlötzer-Schrehardt, Volker Enzmann, Kristian Franze, Stefanie M. Hauck, Antje Grosche. *Investigation*: Lew Kaplan, Corinne Drexler, Anna M. Pfaller, Stefanie M. Hauck, Antje Grosche. *Visualization*: Lew Kaplan, Antje Grosche. *Supervision*: Peter Fuchs, Berta Puig, Kristian Franze, Stefanie M. Hauck, Antje Grosche. *Writing—original draft*: Lew Kaplan, Antje Grosche. *Writing—review & editing*: Lew Kaplan, Volker Enzmann, Marijana Samardzija, Peter Fuchs, Berta Puig, Kristian Franze, Stefanie M. Hauck, Antje Grosche.

CONFLICT OF INTEREST

The authors declare that they have no competing interests.

DATA AVAILABILITY STATEMENT

All data relevant to this work are included in the manuscript and supplemental data. The raw data of the proteomic analysis (e.g., for cell types from all-cone mice, human retina, MIO-M1 cell lysate, and secretome) will be provided by the authors upon request.

ORCID

Lew Kaplan https://orcid.org/0000-0003-4336-2768
Santra Brenna https://orcid.org/0000-0001-8233-2110
Volker Enzmann https://orcid.org/0000-0003-4384-4855
Antje Grosche https://orcid.org/0000-0003-0338-7530

REFERENCES

Adams, M. K., Belyaeva, O. V., Wu, L., & Kedishvili, N. Y. (2014). The retinaldehyde reductase activity of dhrs3 is reciprocally activated by retinol dehydrogenase 10 to control retinoid homeostasis. *The Journal of Biological Chemistry*, *289*, 14868–14880.

Akhmanova, M., Osidak, E., Domogatsky, S., Rodin, S., & Domogatskaya, A. (2015). Physical, spatial, and molecular aspects of extracellular matrix of In vivo niches and artificial scaffolds relevant to stem cells research. *Stem Cells International*, *2015*, 1–35.

Altmann, C., & Schmidt, M. (2018). The role of microglia in diabetic retinopathy: Inflammation, microvasculature defects and neurodegeneration. *International Journal of Molecular Sciences*, *19*, 110.

Bachmann, M., Kukkurainen, S., Hytönen, V. P., & Wehrle-Haller, B. (2019). Cell adhesion by Integrins. *Physiological Reviews*, 99, 1655–1699.

Balmer, J. E., & Blomhoff, R. (2002). Gene expression regulation by retinoic acid. *Journal of Lipid Research*, 43, 1773–1808.

Belyaeva, O. V., Adams, M. K., Popov, K. M., & Kedishvili, N. Y. (2019). Generation of retinaldehyde for retinoic acid biosynthesis. *Biomolecules*, 10, 5.

Benchling. (2021). Cloud-based informatics platform for life sciences R&D | Benchling.

Bhutto, I., & Lutty, G. (2012). Understanding age-related macular degeneration (AMD): Relationships between the photoreceptor/retinal pigment epithelium/Bruch's membrane/choriocapillaris complex. *Molecular Aspects of Medicine*, 33, 295–317.

Billings, S. E., Pierzchalski, K., Tjaden, N. E. B., Pang, X.-Y., Trainor, P. A., Kane, M. A., & Moise, A. R. (2013). The retinaldehyde reductase DHRS3 is essential for preventing the formation of excess retinoic acid during embryonic development. *The FASEB Journal*, 27, 4877–4889.

Bollmann, L., Koser, D. E., Shahapure, R., Gautier, H. O. B., Holzapfel, G. A., Scarcelli, G., Gather, M. C., Ulbricht, E., & Franze, K. (2015). Microglia mechanics: Immune activation alters traction forces and durotaxis. *Frontiers in Cellular Neuroscience*, 9, 363.

Bourgot, I., Primac, I., Louis, T., Noël, A., & Maquoi, E. (2020). Reciprocal interplay between Fibrillar collagens and collagen-binding Integrins: Implications in cancer progression and metastasis. *Frontiers in Oncology*, 10, 1488.

Bringmann, A., Syrbe, S., Görner, K., Kacza, J., Francke, M., Wiedemann, P., & Reichenbach, A. (2018). The primate fovea: Structure, function and development. *Progress in Retinal and Eye Research*, 66, 49–84.

Bringmann, A., Unterlauft, J. D., Wiedemann, R., Barth, T., Rehak, M., & Wiedemann, P. (2020). Two different populations of Müller cells stabilize the structure of the fovea: An optical coherence tomography study. *International Ophthalmology*, 40, 2931–2948.

Bringmann, A., Unterlauft, J. D., Wiedemann, R., Barth, T., Rehak, M., & Wiedemann, P. (2021). Degenerative lamellar macular holes: Tractional development and morphological alterations. *International Ophthalmology*, 41, 1203–1221.

Brunner, A.-D., Thielert, M., Vasilopoulou, C., Ammar, C., Coscia, F., Mund, A., Hoerning, O. B., Bache, N., Apalategui, A., Lubeck, M., Richter, S., Fischer, D. S., Raether, O., Park, M. A., Meier, F., Theis, F. J., & Mann, M. (2022). Ultra-high sensitivity mass spectrometry quantifies single-cell proteome changes upon perturbation. *Molecular Systems Biology*, 18, e10798.

Chambers, D. C., Carew, A. M., Lukowski, S. W., & Powell, J. E. (2019). Transcriptomics and single-cell RNA-sequencing. *Respirology*, 24, 29–36.

Cowan, C. S., Renner, M., De Gennaro, M., Gross-Scherf, B., Goldblum, D., Hou, Y., Munz, M., Rodrigues, T. M., Krol, J., Szikra, T., Papasaikas, P., Cuttat, R., Waldt, A., Diggelmann, R., Patino-Alvarez, C. P., Gerber-Hollbach, N., Schuierer, S., Hou, Y., Srdanovic, A., ... Roska, B. (2020). Cell types of the human retina and its organoids at single-cell resolution. *Cell*, 182, 1623–1640.e34.

da Silva, S., & Cepko, C. L. (2017). Fgf8 expression and degradation of retinoic acid are required for patterning a high-acuity area in the retina. *Developmental Cell*, 42, 68–81.e6.

Domdei, N., Reiniger, J. L., Holz, F. G., & Harmening, W. M. (2021). The relationship between visual sensitivity and eccentricity, cone density and outer segment length in the human Foveola. *Investigative Ophthalmology & Visual Science*, 62, 31.

Doncheva, N. T., Morris, J. H., Gorodkin, J., & Jensen, L. J. (2019). Cytoscape StringApp: Network analysis and visualization of proteomics data. *Journal of Proteome Research*, 18, 623–632.

Escola, J. M., Kleijmeer, M. J., Stoorvogel, W., Griffith, J. M., Yoshie, O., & Geuze, H. J. (1998). Selective enrichment of tetraspan proteins on the internal vesicles of multivesicular endosomes and on exosomes secreted by human B-lymphocytes. *The Journal of Biological Chemistry*, 273, 20121–20127.

Ferrara, M., Lugano, G., Sandinha, M. T., Kearns, V. R., Geraghty, B., & Steel, D. H. W. (2021). Biomechanical properties of retina and choroid: A comprehensive review of techniques and translational relevance. *Eye*, 35, 1818–1832.

Franz, J., Brinkmann, B. F., König, M., Hüve, J., Stock, C., Ebnet, K., & Riethmüller, C. (2016). Nanoscale imaging reveals a Tetraspanin-CD9 coordinated elevation of endothelial ICAM-1 clusters. *PLoS One*, 11, e0146598.

Franze, K., Grosche, J., Skatchkov, S. N., Schinkinger, S., Foja, C., Schild, D., Uckermann, O., Travis, K., Reichenbach, A., & Guck, J. (2007). Müller cells are living optical fibers in the vertebrate retina. *Proceedings of the National Academy of Sciences*, 104, 8287–8292.

Gantner, M. L., Eade, K., Wallace, M., Handzlik, M. K., Fallon, R., Trombley, J., Bonelli, R., Giles, S., Harkins-Perry, S., Heeren, T. F. C., Sauer, L., Ideguchi, Y., Baldini, M., Scheppke, L., Dorrell, M. I., Kitano, M., Hart, B. J., Cai, C., Nagasaki, T., ... Friedlander, M. (2019). Serine and lipid metabolism in macular disease and peripheral neuropathy. *The New England Journal of Medicine*, 381, 1422–1433.

Ghaseminejad, F., Kaplan, L., Pfaller, A. M., Hauck, S. M., & Grosche, A. (2020). The role of Müller cell glucocorticoid signaling in diabetic retinopathy. *Graefe's Archive for Clinical and Experimental Ophthalmology*, 258, 221–230.

Goldman, D. (2014). Müller glial cell reprogramming and retina regeneration. *Nature Reviews. Neuroscience*, 15, 431–442.

Goto, M., Sumiyoshi, H., Sakai, T., Fassler, R., Ohashi, S., Adachi, E., Yoshioka, H., & Fujiwara, S. (2006). Elimination of Epiplakin by gene targeting results in acceleration of keratinocyte migration in mice. *Molecular and Cellular Biology*, 26, 548–558.

Grosche, A., Hauser, A., Lepper, M. F., Mayo, R., von Toerne, C., Merl-Pham, J., & Hauck, S. M. (2016). The proteome of native adult Müller glial cells from murine retina. *Molecular & Cellular Proteomics*, 15, 462–480.

Handa, J. T. (2012). How does the macula protect itself from oxidative stress? *Molecular Aspects of Medicine*, 33, 418–435.

Hao, Y., Hao, S., Andersen-Nissen, E., Mauck, W. M., Zheng, S., Butler, A., Lee, M. J., Wilk, A. J., Darby, C., Zager, M., Hoffman, P., Stoeckius, M., Papalexi, E., Mimitou, E. P., Jain, J., Srivastava, A., Stuart, T., Fleming, L. M., Yeung, B., ... Satija, R. (2021). Integrated analysis of multimodal single-cell data. *Cell*, 184, 3573–3587.e29.

Heeren, T. F. C., Chew, E. Y., Clemons, T., Fruttiger, M., Balaskas, K., Schwartz, R., Egan, C. A., & Charbel Issa, P. (2020). Macular telangiectasia type 2: Visual acuity, disease end stage, and the MacTel area. *Ophthalmology*, 127, 1539–1548.

Hoon, M., Okawa, H., Della Santina, L., & Wong, R. O. L. (2014). Functional architecture of the retina: Development and disease. *Progress in Retinal and Eye Research*, 42, 44–84.

Hu, L., Huang, Z., Wu, Z., Ali, A., & Qian, A. (2018). Mammalian plakins, giant cytolinkers: Versatile biological functions and roles in cancer. *International Journal of Molecular Sciences*, 19, 974.

Hurley, J. B., Lindsay, K. J., & Du, J. (2015). Glucose, lactate, and shuttling of metabolites in vertebrate retinas. *Journal of Neuroscience Research*, 93, 1079–1092.

Hutmacher, F. (2019). Why is there so much more research on vision than on any other sensory modality? *Frontiers in Psychology*, 10, 2246.

Inaba, Y., Chauhan, V., van Loon, A. P., Choudhury, L. S., & Sagasti, A. (2020). Keratins and the plakin family cytolinker proteins control the length of epithelial microridge protrusions. *eLife*, 9, 1–27.

Ishikawa, K., Furuhashi, M., Sasaki, T., Kudoh, J., Tsuchisaka, A., Hashimoto, T., Sasaki, T., Yoshioka, H., Eshima, N., Matsuda-Hirose, H., Sakai, T., Hatano, Y., & Fujiwara, S. (2018). Intragenic copy number variation within human epiplakin 1 (EPPK1) generates variation of molecular size of epiplakin. *Journal of Dermatological Science*, 91, 228–231.

Jang, S.-I., Kalinin, A., Takahashi, K., Marekov, L. N., & Steinert, P. M. (2005). Characterization of human epiplakin: RNAi-mediated epiplakin depletion leads to the disruption of keratin and vimentin IF networks. *Journal of Cell Science*, 118, 781–793.

Janssen, A. F. J., Breusegem, S. Y., & Larrieu, D. (2022). Current methods and pipelines for image-based quantitation of nuclear shape and nuclear envelope abnormalities. *Cell*, 11, 347.

Jones, T. R., Kang, I. H., Wheeler, D. B., Lindquist, R. A., Papallo, A., Sabatini, D. M., Golland, P., & Carpenter, A. E. (2008). CellProfiler analyst: Data exploration and analysis software for complex image-based screens. *BMC Bioinformatics*, 9, 482.

Käll, L., Canterbury, J. D., Weston, J., Noble, W. S., & MacCoss, M. J. (2007). Semi-supervised learning for peptide identification from shotgun proteomics datasets. *Nature Methods*, 4, 923–925.

Kam, R. K. T., Deng, Y., Chen, Y., & Zhao, H. (2012). Retinoic acid synthesis and functions in early embryonic development. *Cell & Bioscience*, 2, 11.

Kassambara A. & Mundt F. (2020). Extract and visualize the results of multivariate data analyses [R package factoextra version 1.0.7].

Kaylor, J. J., Yuan, Q., Cook, J., Sarfare, S., Makshanoff, J., Miu, A., Kim, A., Kim, P., Habib, S., Roybal, C. N., Xu, T., Nusinowitz, S., & Travis, G. H. (2013). Identification of DES1 as a vitamin a isomerase in Müller glial cells of the retina. *Nature Chemical Biology*, 9, 30–36.

Kelly, R. T. (2020). Single-cell proteomics: Progress and prospects. *Molecular & Cellular Proteomics*, 19, 1739–1748.

Kolb H. (1995). Photoreceptors University of Utah Health Sciences Center.

Kolde R. (2019). CRAN - Package pheatmap.

Lenis, T. L., Hu, J., Ng, S. Y., Jiang, Z., Sarfare, S., Lloyd, M. B., Esposito, N. J., Samuel, W., Jaworski, C., Bok, D., Finnemann, S. C., Radeke, M. J., Redmond, T. M., Travis, G. H., & Radu, R. A. (2018). Expression of ABCA4 in the retinal pigment epithelium and its implications for stargardt macular degeneration. *Proceedings of the National Academy of Sciences of the United States of America*, 115, E11120–E11127.

Limb, G. A., Salt, T. E., Munro, P. M. G., Moss, S. E., & Khaw, P. T. (2002). In vitro characterization of a spontaneously immortalized human Müller cell line (MIO-M1). *Investigative Ophthalmology & Visual Science*, 43, 864–869.

Liu, L., MacKenzie, K. R., Putluri, N., Maletić-Savatić, M., & Bellen, H. J. (2017). The glia-neuron lactate shuttle and elevated ROS promote lipid synthesis in neurons and lipid droplet accumulation in glia via APOE/D. *Cell Metabolism*, 26, 719–737.e6.

Liu, Y., Beyer, A., & Aebersold, R. (2016). On the dependency of cellular protein levels on mRNA abundance. *Cell*, 165, 535–550.

Lobo, J., See, E. Y.-S., Biggs, M., & Pandit, A. (2016). An insight into morphometric descriptors of cell shape that pertain to regenerative medicine. *Journal of Tissue Engineering and Regenerative Medicine*, 10, 539–553.

Lowe, D. G. (2004). Distinctive image features from scale-invariant Keypoints. *International Journal of Computer Vision*, 60, 91–110.

Lu, Y.-B., Franze, K., Seifert, G., Steinhäuser, C., Kirchhoff, F., Wolburg, H., Guck, J., Janmey, P., Wei, E.-Q., Käs, J., & Reichenbach, A. (2006). Viscoelastic properties of individual glial cells and neurons in the CNS. *Proceedings of the National Academy of Sciences of the United States of America*, 103, 17759–17764.

MacDonald, R. B., Randlett, O., Oswald, J., Yoshimatsu, T., Franze, K., & Harris, W. A. (2015). Müller glia provide essential tensile strength to the developing retina. *The Journal of Cell Biology*, 210, 1075–1083.

Mages, K., Grassmann, F., Jägle, H., Rupprecht, R., Weber, B. H. F., Hauck, S. M., & Grosche, A. (2019). The agonistic TSPO ligand XBD173 attenuates the glial response thereby protecting inner retinal neurons in a murine model of retinal ischemia. *Journal of Neuroinflammation*, 16, 43.

Margiotta, A., & Bucci, C. (2016). Role of intermediate filaments in vesicular traffic. *Cell*, 5, 20.

McQuin, C., Goodman, A., Chernyshev, V., Kamentsky, L., Cimini, B. A., Karhohs, K. W., Doan, M., Ding, L., Rafelski, S. M., Thirstrup, D., Wiegraebe, W., Singh, S., Becker, T., Caicedo, J. C., & Carpenter, A. E. (2018). CellProfiler 3.0: Next-generation image processing for biology. *PLoS Biology*, 16, e2005970.

Naito, Y., Hino, K., Bono, H., & Ui-Tei, K. (2015). CRISPRdirect: Software for designing CRISPR/Cas guide RNA with reduced off-target sites. *Bioinformatics*, 31, 1120–1123.

Napoli, J. L. (2012). Physiological insights into all-trans-retinoic acid biosynthesis. *Biochimica et Biophysica Acta, Molecular and Cell Biology of Lipids*, 1821, 152–167.

Navarro, P., Trevisan-Herraz, M., Bonzon-Kulichenko, E., Núñez, E., Martínez-Acedo, P., Pérez-Hernández, D., Jorge, I., Mesa, R., Calvo, E., Carrascal, M., Hernáez, M. L., García, F., Bárcena, J. A., Ashman, K., Abian, J., Gil, C., Redondo, J. M., & Vázquez, J. (2014). General statistical framework for quantitative proteomics by stable isotope labeling. *Journal of Proteome Research*, 13, 1234–1247.

Noya, S. B., Colameo, D., Brüning, F., Spinnler, A., Mircsof, D., Opitz, L., Mann, M., Tyagarajan, S. K., Robles, M. S., & Brown, S. A. (2019). The forebrain synaptic transcriptome is organized by clocks but its proteome is driven by sleep. *Science (80-)*, 366, eaav2642.

Pannicke, T., Wagner, L., Reichenbach, A., & Grosche, A. (2018). Electrophysiological characterization of Müller cells from the ischemic retina of mice deficient in the leukemia inhibitory factor. *Neuroscience Letters*, 670, 69–74.

Pauly, D., Agarwal, D., Dana, N., Schäfer, N., Biber, J., Wunderlich, K. A., Jabri, Y., Straub, T., Zhang, N. R., Gautam, A. K., Weber, B. H. F., Hauck, S. M., Kim, M., Curcio, C. A., Stambolian, D., Li, M., & Grosche, A. (2019). Cell-type-specific complement expression in the healthy and diseased retina. *Cell Reports*, 29, 2835–2848.e4.

Potokar, M., Kreft, M., Li, L., Daniel Andersson, J., Pangršič, T., Chowdhury, H. H., Pekny, M., & Zorec, R. (2007). Cytoskeleton and vesicle mobility in astrocytes. *Traffic*, 8, 12–20.

Potokar, M., Morita, M., Wiche, G., & Jorgačevski, J. (2020). The diversity of intermediate filaments in astrocytes. *Cell*, 9, 1604.

Ran, F. A., Hsu, P. D., Wright, J., Agarwala, V., Scott, D. A., & Zhang, F. (2013). Genome engineering using the CRISPR-Cas9 system. *Nature Protocols*, 8, 2281–2308.

Reichenbach, A., & Bringmann, A. (2020). Glia of the human retina. *Glia*, 68, 768–796.

Reyes, R., Cardeñes, B., Machado-Pineda, Y., & Cabañas, C. (2018). Tetraspanin CD9: A key regulator of cell adhesion in the immune system. *Frontiers in Immunology*, 9, 863.

Ritchie, M. E., Phipson, B., Wu, D., Hu, Y., Law, C. W., Shi, W., & Smyth, G. K. (2015). Limma powers differential expression analyses for RNA-sequencing and microarray studies. *Nucleic Acids Research*, 43, e47.

Samardzija, M., Caprara, C., Heynen, S. R., DeParis, S. W., Meneau, I., Traber, G., Agca, C., von Lintig, J., & Grimm, C. (2014). A mouse model for studying cone photoreceptor pathologies. *Investigative Ophthalmology and Visual Science*, 55, 5304–5313.

Samardzija, M., Von lintig, J., Tanimoto, N., Oberhauser, V., Thiersch, M., Seeliger, M., Remé, C. E., Grimm, C., & Wenzel, A. (2008). R91W mutation in Rpe65 leads to milder early-onset retinal dystrophy due to the generation of low levels of 11-cis-retinal. *Human Molecular Genetics*, 17, 281–292.

Scerri, T. S., Quaglieri, A., Cai, C., Zernant, J., Matsunami, N., Baird, L., Scheppke, L., Bonelli, R., Yannuzzi, L. A., Friedlander, M., MacTel Project Consortium, Egan, C. A., Fruttiger, M., Leppert, M., Allikmets, R., & Bahlo, M. (2017). Genome-wide analyses identify common variants associated with macular telangiectasia type 2. *Nature Genetics*, 49, 559–567.

Schindelin, J., Arganda-Carreras, I., Frise, E., Kaynig, V., Longair, M., Pietzsch, T., Preibisch, S., Rueden, C., Saalfeld, S., Schmid, B., Tinevez, J. Y., White, D. J., Hartenstein, V., Eliceiri, K., Tomancak, P., &

Cardona, A. (2012). Fiji: An open-source platform for biological-image analysis. *Nature Methods*, 9, 676–682.

Shannon, P., Markiel, A., Ozier, O., Baliga, N. S., Wang, J. T., Ramage, D., Amin, N., Schwikowski, B., & Ideker, T. (2003). Cytoscape: A software environment for integrated models of biomolecular interaction networks. *Genome Research*, 13, 2498–2504.

Sharma, K., Schmitt, S., Bergner, C. G., Tyanova, S., Kannaiyan, N., Manrique-Hoyos, N., Kongi, K., Cantuti, L., Hanisch, U.-K., Philips, M.-A., Rossner, M. J., Mann, M., & Simons, M. (2015). Cell type- and brain region-resolved mouse brain proteome. *Nature Neuroscience*, 18, 1819–1831.

Slezak, M., Grosche, A., Niemiec, A., Tanimoto, N., Pannicke, T., Münch, T. A., Crocker, B., Isope, P., Härtig, W., Beck, S. C., Huber, G., Ferracci, G., Perraut, M., Reber, M., Miehe, M., Demais, V., Lévêque, C., Metzger, D., Szklarczyk, K., ... Pfrieger, F. W. (2012). Relevance of Exocytotic glutamate release from retinal glia. *Neuron*, 74, 504–516.

Sonnenberg, A., & Liem, R. K. H. (2007). Plakins in development and disease. *Experimental Cell Research*, 313, 2189–2203.

Spazierer, D., Fuchs, P., Pröll, V., Janda, L., Oehler, S., Fischer, I., Hauptmann, R., & Wiche, G. (2003). Epiplakin gene analysis in mouse reveals a single exon encoding a 725-kDa protein with expression restricted to epithelial tissues. *The Journal of Biological Chemistry*, 278, 31657–31666.

Spazierer, D., Fuchs, P., Reipert, S., Fischer, I., Schmuth, M., Lassmann, H., & Wiche, G. (2006). Epiplakin is dispensable for skin barrier function and for integrity of keratin network cytoarchitecture in simple and stratified epithelia. *Molecular and Cellular Biology*, 26, 559–568.

Spazierer, D., Raberger, J., Groß, K., Fuchs, P., & Wiche, G. (2008). Stress-induced recruitment of epiplakin to keratin networks increases their resistance to hyperphosphorylation-induced disruption. *Journal of Cell Science*, 121, 825–833.

Stuart, T., Butler, A., Hoffman, P., Hafemeister, C., Papalexi, E., Mauck, W. M., Hao, Y., Stoeckius, M., Smibert, P., & Satija, R. (2019). Comprehensive integration of single-cell data. *Cell*, 177, 1888–1902.e21.

Syrbe, S., Kuhrt, H., Gärtner, U., Habermann, G., Wiedemann, P., Bringmann, A., & Reichenbach, A. (2018). Müller glial cells of the primate foveola: An electron microscopical study. *Experimental Eye Research*, 167, 110–117.

Szabo, S., Wögenstein, K. L., Österreicher, C. H., Guldiken, N., Chen, Y., Doler, C., Wiche, G., Boor, P., Haybaeck, J., Strnad, P., & Fuchs, P. (2015). Epiplakin attenuates experimental mouse liver injury by chaperoning keratin reorganization. *Journal of Hepatology*, 62, 1357–1366.

Théry, C., Regnault, A., Garin, J., Wolfers, J., Zitvogel, L., Ricciardi-Castagnoli, P., Raposo, G., & Amigorena, S. (1999). Molecular characterization of dendritic cell-derived exosomes: Selective accumulation of the heat shock protein hsc73. *The Journal of Cell Biology*, 147, 599–610.

Théry, C., Witwer, K. W., Aikawa, E., Alcaraz, M. J., Anderson, J. D., Andriantsitohaina, R., Antoniou, A., Arab, T., Archer, F., Atkin-Smith, G. K., Ayre, D. C., Bach, J. M., Bachurski, D., Baharvand, H., Balaj, L., Baldacchino, S., Bauer, N. N., Baxter, A. A., Bebawy, M., ... Zuba-Surma, E. K. (2018). Minimal information for studies of extracellular vesicles 2018 (MISEV2018): A position statement of the International Society for Extracellular Vesicles and update of the MISEV2014 guidelines. *Journal of Extracellular Vesicles*, 7, 1535750.

Thompson, B., Katsanis, N., Apostolopoulos, N., Thompson, D. C., Nebert, D. W., & Vasiliou, V. (2019). Genetics and functions of the retinoic acid pathway, with special emphasis on the eye. *Human Genomics*, 13, 61.

Toft-Kehler, A. K., Skytt, D. M., & Kolko, M. (2018). A perspective on the Müller cell-neuron metabolic partnership in the inner retina. *Molecular Neurobiology*, 55, 5353–5361.

Tonoike, Y., Matsushita, K., Tomonaga, T., Katada, K., Tanaka, N., Shimada, H., Nakatani, Y., Okamoto, Y., & Nomura, F. (2011). Adhesion molecule periplakin is involved in cellular movement and attachment in pharyngeal squamous cancer cells. *BMC Cell Biology*, 12, 41.

Tschulakow, A. V., Oltrup, T., Bende, T., Schmelzle, S., & Schraermeyer, U. (2018). The anatomy of the foveola reinvestigated. *PeerJ*, 6, e4482.

Tseng Q. (2011). Etude d'architecture multicellulaire avec le microenvironnement contrôlé.

Tseng, Q., Duchemin-Pelletier, E., Deshiere, A., Balland, M., Guilloud, H., Filhol, O., & Théry, M. (2012). Spatial organization of the extracellular matrix regulates cell-cell junction positioning. *Proceedings of the National Academy of Sciences of the United States of America*, 109, 1506–1511.

Ueo, D., Furuhashi, M., Sasaki, T., Kudoh, J., Parry, D. A. D., Winter, D. J., Sasaki, T., Hashimoto, T., Tsuruta, D., & Fujiwara, S. (2021). Intragenic copy number variation in mouse epiplakin 1 (Eppk1) and the conservation of the repeat structures in the lower vertebrates. *Journal of Dermatological Science*, 103, 186–189.

Verbakel, S. K., van Huet, R. A. C., Boon, C. J. F., den Hollander, A. I., Collin, R. W. J., Klaver, C. C. W., Hoyng, C. B., Roepman, R., & Klevering, B. J. (2018). Non-syndromic retinitis pigmentosa. *Progress in Retinal and Eye Research*, 66, 157–186.

Vogel, C., & Marcotte, E. M. (2012). Insights into the regulation of protein abundance from proteomic and transcriptomic analyses. *Nature Reviews. Genetics*, 13, 227–232.

Voigt, A. P., Mullin, N. K., Stone, E. M., Tucker, B. A., Scheetz, T. E., & Mullins, R. F. (2021). Single-cell RNA sequencing in vision research: Insights into human retinal health and disease. *Progress in Retinal and Eye Research*, 83, 100934.

Voigt, A. P., Whitmore, S. S., Flamme-Wiese, M. J., Riker, M. J., Wiley, L. A., Tucker, B. A., Stone, E. M., Mullins, R. F., & Scheetz, T. E. (2019). Molecular characterization of foveal versus peripheral human retina by single-cell RNA sequencing. *Experimental Eye Research*, 184, 234–242.

Wan, J., & Goldman, D. (2016). Retina regeneration in zebrafish. *Current Opinion in Genetics & Development*, 40, 41–47.

Wang, J. S., & Kefalov, V. J. (2009). An alternative pathway mediates the mouse and human cone visual cycle. *Current Biology*, 19, 1665–1669.

Wang, J.-S., & Kefalov, V. J. (2011). The cone-specific visual cycle. *Progress in Retinal and Eye Research*, 30, 115–128.

Wang, W., Sumiyoshi, H., Yoshioka, H., & Fujiwara, S. (2006). Interactions between epiplakin and intermediate filaments. *The Journal of Dermatology*, 33, 518–527.

Wässle, H., Haverkamp, S., & Grünert, U. (2002). The cone pedicle a complex synapse in the retina. *The Keio Journal of Medicine*, 51, 19–20.

Whitmore, S. S., Wagner, A. H., DeLuca, A. P., Drack, A. V., Stone, E. M., Tucker, B. A., Zeng, S., Braun, T. A., Mullins, R. F., & Scheetz, T. E. (2014). Transcriptomic analysis across nasal, temporal, and macular regions of human neural retina and RPE/choroid by RNA-Seq. *Experimental Eye Research*, 129, 93–106.

Wiśniewski, J. R., Zougman, A., Nagaraj, N., & Mann, M. (2009). Universal sample preparation method for proteome analysis. *Nature Methods*, 65(6), 359–362.

Wögenstein, K. L., Szabo, S., Lunova, M., Wiche, G., Haybaeck, J., Strnad, P., Boor, P., Wagner, M., & Fuchs, P. (2014). Epiplakin deficiency aggravates murine caerulein-induced acute pancreatitis and favors the formation of acinar keratin granules. *PLoS One*, 9, e108323.

Wunderlich, K. A., Tanimoto, N., Grosche, A., Zrenner, E., Pekny, M., Reichenbach, A., Seeliger, M. W., Pannicke, T., & Perez, M.-T. (2015). Retinal functional alterations in mice lacking intermediate filament proteins glial fibrillary acidic protein and vimentin. *The FASEB Journal*, 29, 4815–4828.

Xue, Y., Sato, S., Razafsky, D., Sahu, B., Shen, S. Q., Potter, C., Sandell, L. L., Corbo, J. C., Palczewski, K., Maeda, A., Hodzic, D., & Kefalov, V. J. (2017). The role of retinol dehydrogenase 10 in the cone visual cycle. *Scientific Reports*, 7, 2390.

Xue, Y., Shen, S. Q., Jui, J., Rupp, A. C., Byrne, L. C., Hattar, S., Flannery, J. G., Corbo, J. C., & Kefalov, V. J. (2015). CRALBP supports the mammalian retinal visual cycle and cone vision. *The Journal of Clinical Investigation*, *125*, 727–738.

Yeo, N. J. Y., Chan, E. J. J., & Cheung, C. (2019). Choroidal neovascularization: Mechanisms of endothelial dysfunction. *Frontiers in Pharmacology*, *10*, 1363.

Yuodelis, C., & Hendrickson, A. (1986). A qualitative and quantitative analysis of the human fovea during development. *Vision Research*, *26*, 847–855.

Zhang, T., Zhu, L., Madigan, M. C., Liu, W., Shen, W., Cherepanoff, S., Zhou, F., Zeng, S., Du, J., & Gillies, M. C. (2019). Human macular Müller cells rely more on serine biosynthesis to combat oxidative stress than those from the periphery. *eLife*, *8*, 1–19.

SUPPORTING INFORMATION

Additional supporting information can be found online in the Supporting Information section at the end of this article.

How to cite this article: Kaplan, L., Drexler, C., Pfaller, A. M., Brenna, S., Wunderlich, K. A., Dimitracopoulos, A., Merl-Pham, J., Perez, M.-T., Schlötzer-Schrehardt, U., Enzmann, V., Samardzija, M., Puig, B., Fuchs, P., Franze, K., Hauck, S. M., & Grosche, A. (2022). Retinal regions shape human and murine Müller cell proteome profile and functionality. *Glia*, 1–24. https://doi.org/10.1002/glia.24283